

Appendix

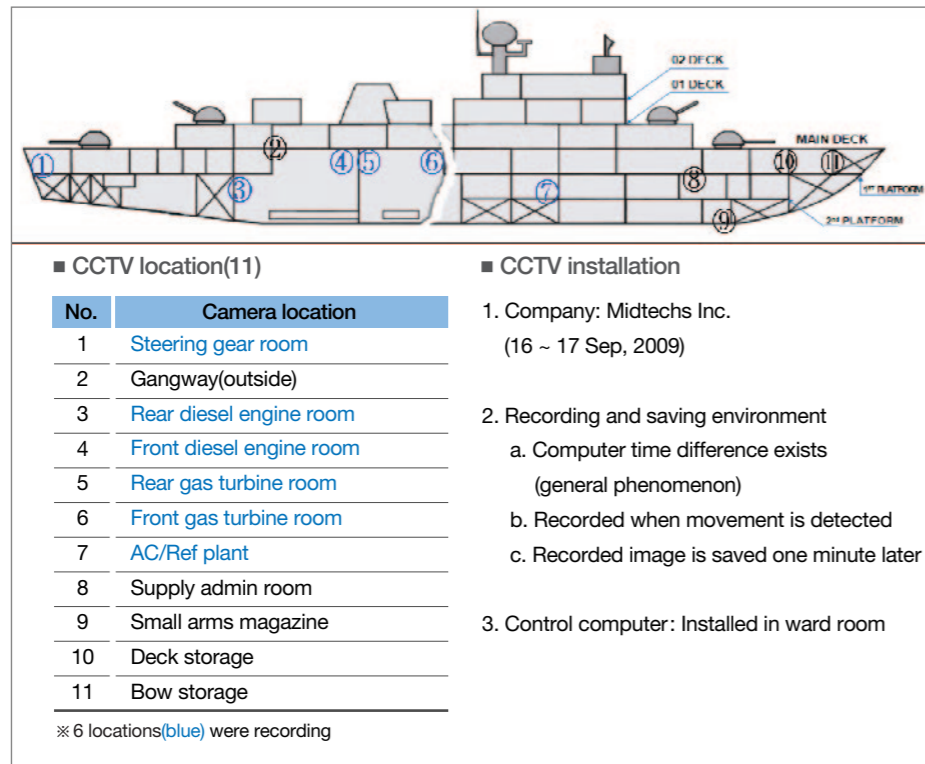
- I. CCTV Recovery and Analysis Result
- II. Underwater Explosion Phenomenon
- III. Analysis Result on Direction and Location of the Explosion
- IV. Analysis Result on Charge Size and Depth
- V. Analysis Result on Adhered Materials
- VI. Stability Analysis Result
- VII. Basic Hull Strength Analysis Result



Appendix I. CCTV Recovery and Analysis Result

1. Overview

In order to facilitate the CCTV analysis, the JIG cooperated with the company that installed the CCTV, and identified locations of the control computers(the ward room), number of internal and external locations of the cameras, and CCTV characteristics. On April 24, during the salvage operation for the bow, the JIG quickly recovered the ones located at the gangway and the gas turbine room, since the prioritization was made upon the assessment that these footages with the records from 2100 on the incident day would assist the most in the efforts to determine the cause of the incident. The JIG also made appointments with a contractor(Myung Information Technology in Oh-chang) that would be responsible for the hard disk recovery process.



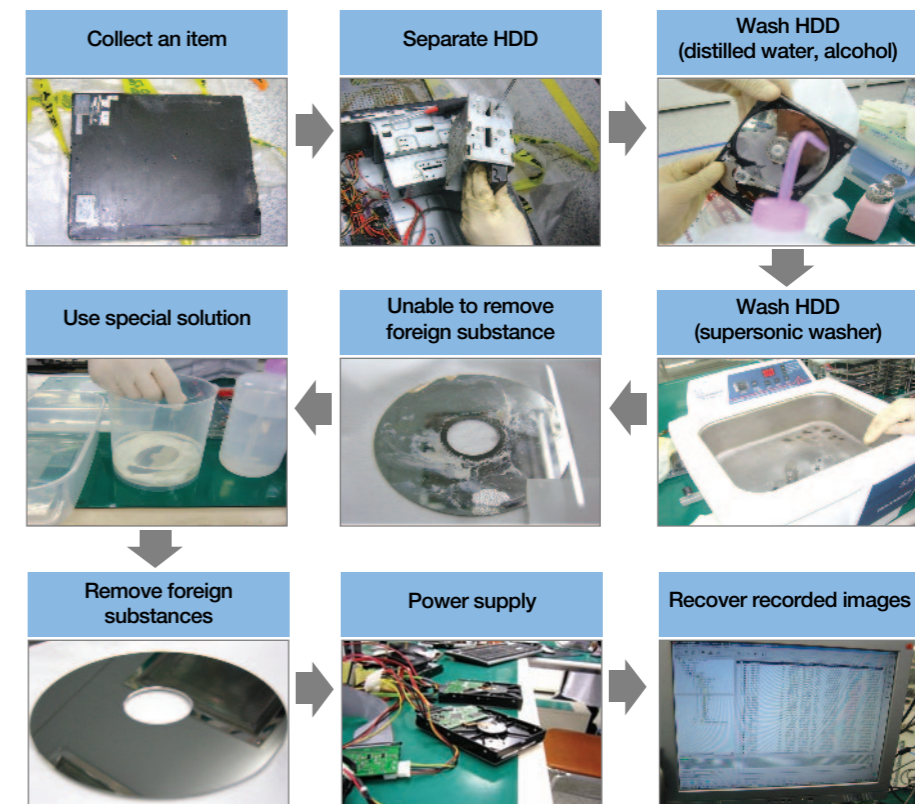
〈Figure Appendix I-1-1〉 ROKS Cheonan CCTV location

2. Procedure of CCTV Recovery Operation

The CCTV recovery operation was hampered due to oil, mud, and other foreign substances that were attached to the hard drive for over a month. Through the spraying of pure alcohol, distilled water and thinners along with ultrasound waves(these are the most effective means for success) for 6 days, the JIG made repeated attempts to remove these substances; however, the attached foreign substances could not be completely removed.

Therefore, a group of experts discussed whether to partially carve out the hard disk's surface, or to melt down the foreign substances as suggested by the JIG analysis team. They assessed that the latter course of action would have a better chance for success, and decided to take a careful approach on this matter.

The JIG requested for a composition analysis on the foreign substance to the KCIC scientific investigation lab. The foreign substance was composed of Al, and NaOH was identified.



〈Figure Appendix I-2-1〉 CCTV recovery process

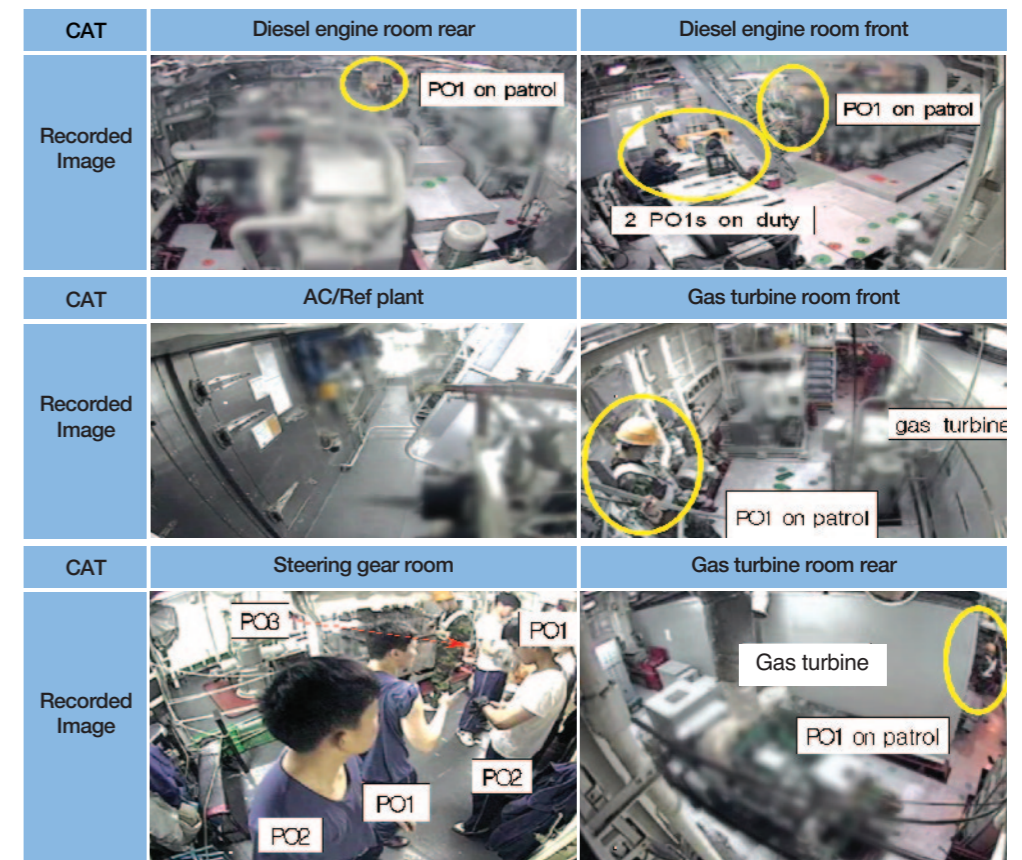
tified as the solution to remove the foreign substances. The melting process took 2 days, and the amount of NaOH solution was increased incrementally to prevent damage to the disk. After dozens of trials, the elimination of the foreign AI from the disk succeeded, and the operation was able to recover partial image of the 6 CCTVs saved in the hard disk, and the image from the other 5 CCTVs were not restored, because there were no movements within the covering area of these CCTVs.

3. Recovery Result

Because of the way the settings were set up for ROKS Cheonan's 11 CCTVs, the initially inserted recording time did not get updated, and this resulted in a time difference with the actual time of recording. The CCTV begins recording when movement is detected, and the images are saved 1 minute after the recording. After taking this setting into account as well as the statements from survivors, the analysis showed that the CCTV that recorded the latest time frame was the one that was located in the gas turbine room, and the JIG estimated it to have halted recording at 2121 hours(21:17:03 on the CCTV time).

No.	Installed locations	Contents of image	Time on screen		
			Start	Finish	Duration
1	Diesel engine room rear(stern)	Safety watch PO1 on patrol	21:12:23	21:13:06	43"
2	Diesel engine room front(stern)	① 2 PO1s on duty ② Safety watch PO1 on patrol	21:02:21	21:13:16	10' 55"
3	AC/Ref plant (bow)	Unable to verify movement due to file damage	21:02:40	21:15:50	13' 10"
4	Gas turbine room front(stern)	Safety watch PO1 on patrol	21:15:20	21:16:12	52"
5	Steering gear room (stern)	① 3(PO1, PO2, PO3) working out ② PO2, PO1 entering ③ Safety watch PO1 on patrol	21:02:20	21:17:01	14' 41"
6	Gas turbine room rear(stern)	Safety watch PO1 on patrol	21:02:20	21:17:03	14' 43"
TOT	6 locations	8 moving personnel	21:02:20	21:17:03	TOT: 55' 04"

〈Table Appendix I-3-1〉 CCTV recovered contents



〈Figure Appendix I-3-1〉 CCTV recorded footage

4. Analysis Result

From the recovery, the images of the gas turbine room and diesel engine room were confirmed, as well as those of the patrolling of a safety watch, and other crew members exercising in the steering gearing room. Based on the routine circumstances in the observed compartments, outfits and facial expressions of crew members, along with stable sailing status, it was concluded that ROKS Cheonan was on normal operations without any emergency situation such as grounding, until a sudden explosion fractured the hull and caused the sinking.

Appendix II. Underwater Explosion Phenomenon

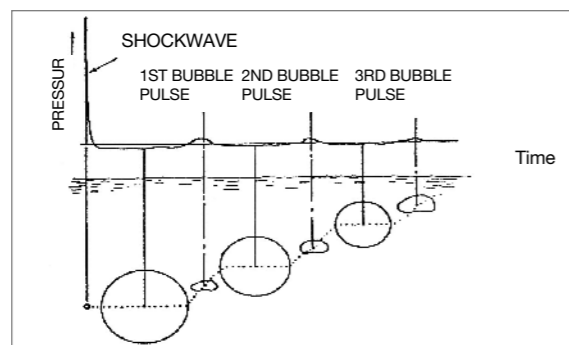
1. Physical Aspects of Underwater Explosion¹⁾

When an explosive charge is detonated underwater, shockwave of extremely high pressure propagates into water, and spherical bubble of high-temperature(2,000~6,000K) and high-pressure(150~400kbar) detonation products are formed. <Figure Appendix II-1-1> shows the pressure of the shockwave and bubble pulses, and process of bubble oscillation, with respect to time. The shockwave generated by an underwater explosion commences to propagate into surrounding water spherically at a high velocity(~7km/s) initially, and soon it slows down to the level of the sound speed(~1.5km/s) as it moves away from the point of detonation. As the shockwave travels, the peak overpressure(P_m) decreases and the duration increases. Therefore, the shockwave pressure depends on the type of explosive, charge weight(W), distance(R), and time(t), as follows:

$$P(R, W; t) = P_m(R, W) \exp\left[-\frac{(t-t_0)}{\theta(R, W)}\right] \quad (1)$$

$$P_m(R, W) = K \left(\frac{W^{1/3}}{R}\right)^{\alpha}, \quad \theta(R, W) = W^{1/3} K' \left(\frac{W^{1/3}}{R}\right)^{\alpha'}$$

where K, α, K', α' are constants having values depending on the types of explosives.



<Figure Appendix II-1-1> Shockwave & bubble pressure-time graph

1) Michael M. Swisdak, "Explosion Effects and Properties : Part II - Explosion Effects in Water", NSWC/WOL TR 76-116, 1978.

As shown in <Figure Appendix II-1-1>, the bubble pulses after the shockwave indicate pressure generated when the gas bubble of detonation products contracts and starts to expand. This bubble process takes place slowly and under relatively low pressure compared to that of the shockwave. Due to high pressure and temperature at the initial stage, the gas bubble pushes water toward outside the spherical surface while expanding. Because of the inertia of the expanding water, the expansion stops after passing the point of pressure equilibrium(hydrostatic pressure at the point of detonation). The bubble at its peak of expansion retains a very low internal pressure of less than about 0.01 atm. Thus, the hydrostatic pressure in the vicinity of the bubble becomes higher than the pressure inside the bubble, and as a result the bubble is forced to contract. Similar to the expansion, the bubble continues to contract even beyond the pressure equilibrium, and the pressure inside the bubble reaches hundreds of atmospheric pressure, much higher than the hydrostatic pressure of the surrounding water. At this moment, the bubble starts to expand again, releasing a pulse of relatively high pressure. While repeating the expansion and contraction, the bubble oscillates. As the bubble pulsation is a very slow process compared with the shockwave propagation, the bubble movement is influenced by gravity, and thus, the bubble jumps toward the water surface when its volume is reduced to its minimum.

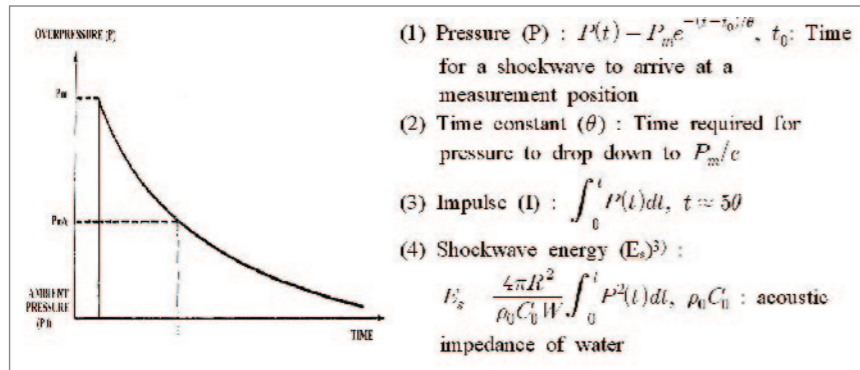
The energy of underwater explosion is partitioned into two parts, the generation and dissipation of the shockwave, and the expansion and contraction of the bubble, as listed in <Table Appendix II-1-1>²⁾. That is, the shockwave energy is lost while radiating spherically and propagating in surrounding water, and the bubble energy is spent through interaction with the water, radiation, and bubble pulse. In case of a shallow-depth underwater explosion, it is known that most of the bubble energy is consumed during the first bubble period.

<Figure Appendix II-1-2> is a magnification of <Figure Appendix II-1-1> and shows important parameters for understanding propagation of an underwater shockwave.

Total energy liberated (100%)	Initial shockwave energy(53~54%)
	Energy in first bubble oscillation(46~47%)

<Table Appendix II-1-1> Energy partition of a bulk warhead fired underwater

2) Warren C. Strahle, "Conventional Weapons Underwater Explosions", AD-A201 814, December 1988.



〈Figure Appendix II-1-2〉 Shockwave parameters

Also, in order to compare UNDEX effects for explosive charges other than TNT, it is necessary to define the terminologies, as listed below:

(1) Equal weight ratio (D _{wd})	The ratio of the outputs of a particular parameter(peak overpressure, time constant, impulse, energy) for equal weights of two explosives at the same distance.	
(2) Equal volume ratio (D _{vd})	The ratio of the outputs of a particular parameter(peak overpressure, time constant, impulse, energy) for equal volumes of two explosives at the same distance.	
(3) Equivalent weight ratio (W _{wd})	The ratio of weights of two explosives required to produce the same magnitude of a particular parameter at the same distance.	
(4) Relative bubble energy (RBE)	Cube of the ratio of the first bubble period constants(K's):	$RBE = \left(\frac{K_{experimental}}{K_{reference}} \right)^3$
(5) Relative potential bubble energy(RPBE)	Cube of the ratio of the maximum bubble radius constants(J's):	$RPBE = \left(\frac{J_{experimental}}{J_{reference}} \right)^3$

1) Characteristics of an Underwater Shockwave

The parameters, P_m, θ, I, E_s which represent the characteristics of shockwave generated by an underwater explosion of a high explosive, depend on the weight(W) of the charge and the distance between the point of the explosion and the measurement location(R), as ex-

3) Robert H. Cole, "Underwater Explosions", Princeton University Press, 1948.

pressed in the following similitude relation⁴⁾:

$$\text{Shock Parameter} = K \left(\frac{W^{1/3}}{R} \right)^\alpha \quad (2)$$

Where constants determined by the type of the explosive charge, R is distance(m) from the explosive charge, and W indicates weight of the explosive charge(kg). 〈Table Appendix II-1-2〉 lists values of constants in the similitude relation, Equation(2), for various explosives. 〈Table Appendix II-1-3〉 summarizes the Equal Weight Ratios applicable to explosive charges over a weight of 20kg. 〈Figure Appendix II-1-3〉 shows peak overpressure(P_m) of the shockwave from various charge weights of TNT with respect to dis-

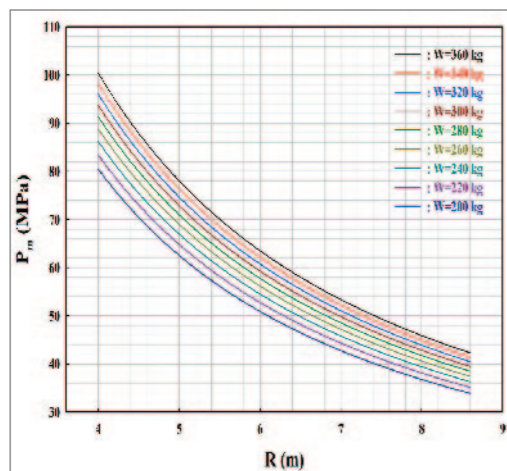
Explosive	Shock parameter		P _m		θW ^{1/3}		1/W ^{1/3}		EW ^{1/3}		Range of validity (MPa)
	K	α	K	α	K	α	K	α			
TNT	52.4	1.13	0.084	-0.23	5.75	0.89	84.4	2.04	3.4-138		
PENTOLITE	56.5	1.14	0.084	-0.23	5.73	0.91	92.0	2.04	3.4-138		
H-6	59.2	1.19	0.088	-0.28	6.58	0.91	115.3	2.08	10.3-138		
HBX-1	56.7	1.15	0.083	-0.29	6.42	0.85	106.2	2.00	3.4-60		
HBX-1	56.1	1.37	0.088	-0.36	6.15	0.95	107.2	2.26	60-500		
HBX-3	50.3	1.14	0.091	-0.218	6.33	0.90	90.9	2.02	3.4-60		
HBX-3	54.3	1.18	0.091	-0.218	6.70	0.80	114.4	1.97	60-350		

〈Table Appendix II-1-2〉 Shockwave constants for various explosives

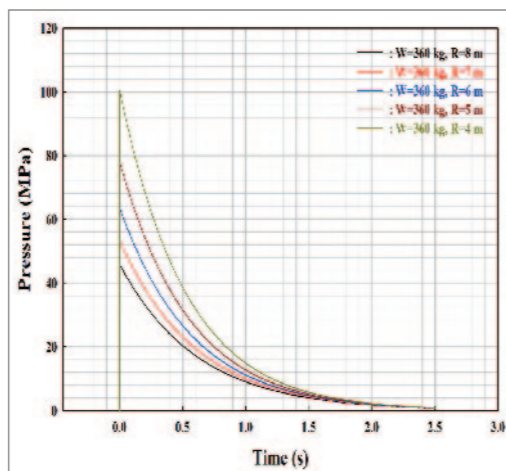
Explosive	Equal weight ratio				Equal weight ratio				(RBE) _{TNT}	(RPBE) _{TNT}
	D _{wd} (relative to HBX-1)				D _{wd} (relative to TNT)					
	P _m	θ	I	E	P _m	θ	I	E		
HBX-1	1.00	1.00	1.00	1.00	1.08	0.99	1.12	1.26	1.48	1.44
TNT	0.92	1.01	0.90	0.79	1.00	1.00	1.00	1.00	1.00	1.00
HBX-3	0.89	1.10	0.99	0.86	0.96	1.08	1.10	1.08	1.93	1.82
H-6	1.04	1.06	1.02	1.09	1.13	1.05	1.14	1.37	1.69	1.59
PENTOLITE	1.00	1.01	0.89	0.87	1.08	1.00	1.00	1.09	1.00	1.02

〈Table Appendix II-1-3〉 Conversion factors between shockwave and bubble

4) Similitude relation: The relation applied to calculate the shock wave factors such as pressure, time constant, shock amount, and shock energy.



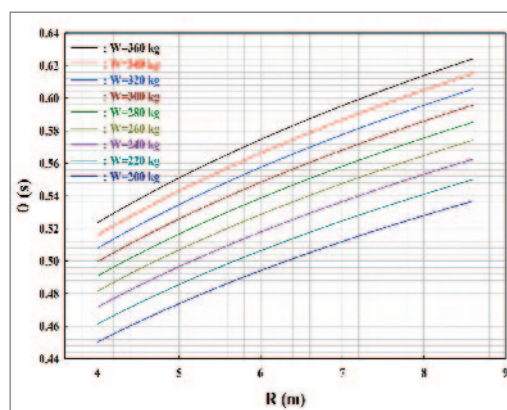
〈Figure Appendix II-1-3〉 Shockwave peak overpressure of various weights of TNT



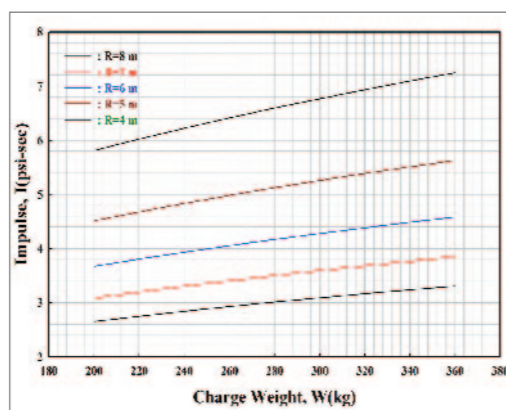
〈Figure Appendix II-1-4〉 Shockwave peak overpressure at several distances from underwater explosion of 250kg TNT

tance(R) from the explosive charge.

In addition, 〈Figure Appendix II-1-4〉 shows the changes in peak overpressure of the shockwave in time at several distances from an underwater explosion of TNT of 250kg. 〈Figure Appendix II-1-5〉 shows the time constant(θ) which implies time required for P(t) to fall from Pm to Pm/e. P(t) and θ are essential data in calculating the impulse ($I = \int_0^{\theta} P(t) dt$). The shockwave impulse from a given charge weight of TNT(W) at distance(R) away from the charge can be obtained from 〈Figure Appendix II-1-6〉.



〈Figure Appendix II-1-5〉 Time constant(θ) for different charge weights



〈Figure Appendix II-1-6〉 Shockwave impulse vs. TNT charge size

2) Characteristics of an Underwater Bubble

The characteristics of an underwater bubble are delineated in the 〈Figure Appendix II-1-1〉, and Willis P.M., based on his experiment, proposed that oscillation period(T) and maximum radius(A_m) of a bubble can be expressed as:

$$T = K \frac{W^{1/3}}{Z^{5/6}} \quad (3)$$

$$A_m = J \frac{W^{1/3}}{Z^{1/3}} \quad (4)$$

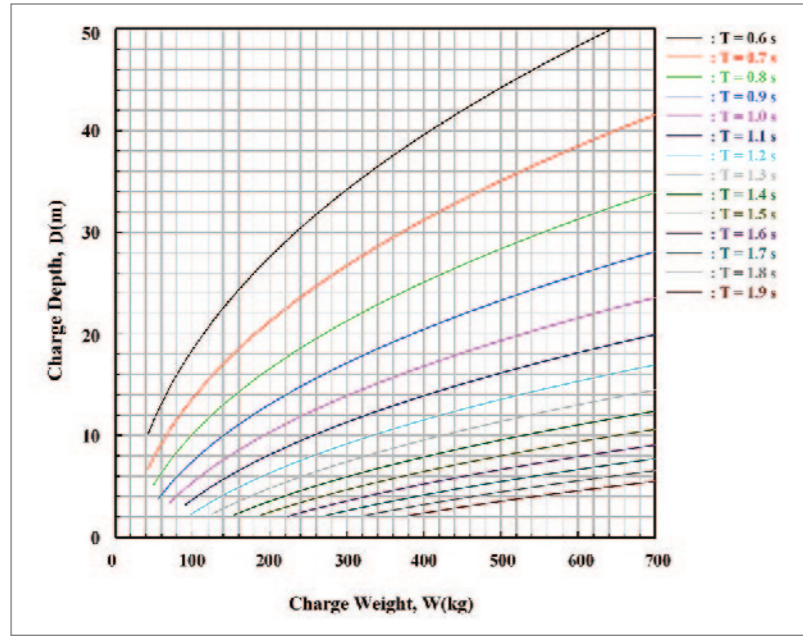
$$Z = 10.1 + D(m)$$

where, K and J are bubble constants determined by the types of explosives, and values obtained from experimental data for selected explosives are listed in 〈Table Appendix II-1-4〉.

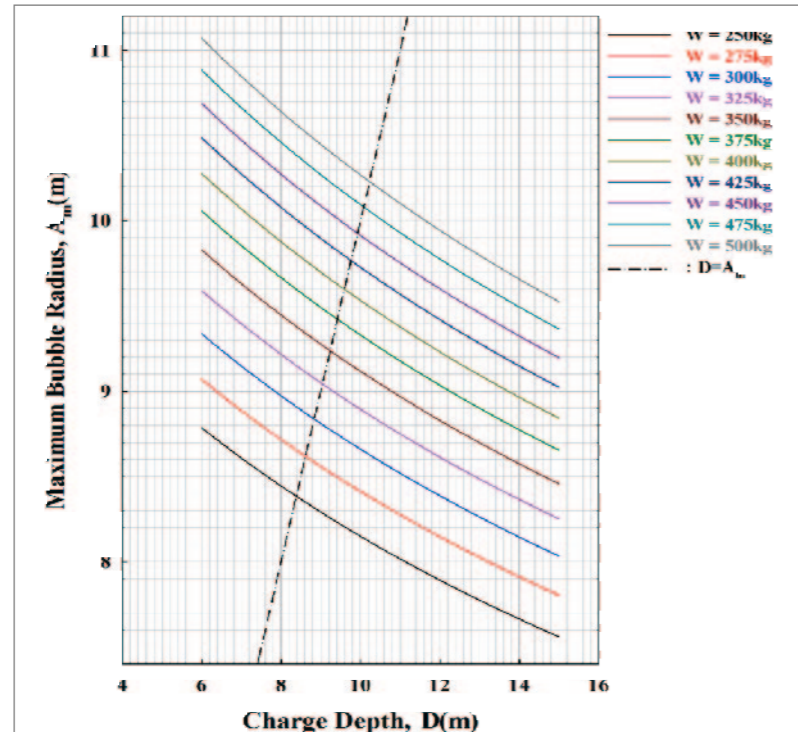
EXPLOSIVE	J	K
TNT	3.50	2.11
PENTOLITE	3.52	2.11
HBX-1	3.95	2.41
HBX-3	4.27	2.63
H-6	4.09	2.52

〈Table Appendix II-1-4〉 Bubble constants for selected explosives

〈Figure Appendix II-1-7〉 and 〈Figure Appendix II-1-8〉 show the bubble period(T) and maximum bubble radius(A_m) for a TNT charge as a function of the depth(D) of the explosive, respectively.



〈Figure Appendix II-1-7〉 Bubble period(T) of the bubble formed by TNT at different depths



〈Figure Appendix II-1-8〉 Maximum bubble radius(A_m) of the bubble formed by TNT at different depths

3) Formation of Water Column and Water Jet generated from Underwater Explosion

Summarized below are the formulas for the maximum height of the water jet, and the maximum diameter of the water column and smoke plume generated from a relatively shallow underwater explosion of TNT at seabed. 〈Figure Appendix II-1-9〉 and 〈Figure Appendix II-1-10〉 are the plots of maximum jet height and maximum column diameter as a function of scaled charge depth.

$$H_{max}/W^{1/3} = 32.4(Y/W^{1/4})^{0.1}, \quad 0.0037 < Y/W^{1/4} < 0.74 \quad (5)$$

$$H_{max}/W^{1/3} = 21.7(Y/W^{1/4})^{-1.24}, \quad 0.74 < Y/W^{1/4} < 1.56$$

$$D_{max}/W^{1/3} = 3.71(Y/W^{1/4})^{0.166}, \quad 0.08 < Y/W^{1/4} < 0.88$$

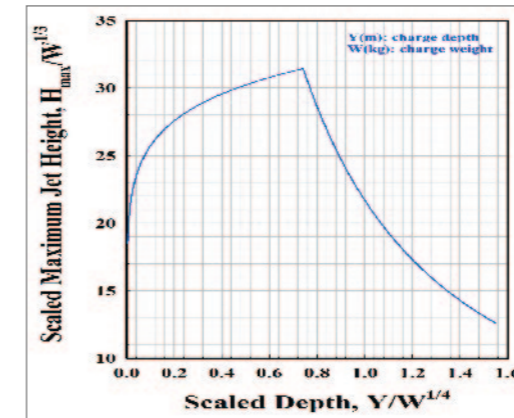
$$S_{max}/W^{1/3} = 9.00$$

$$H_{max}/W^{1/3} = \text{scaled maximum jet height (m/kg}^{1/3}\text{)}$$

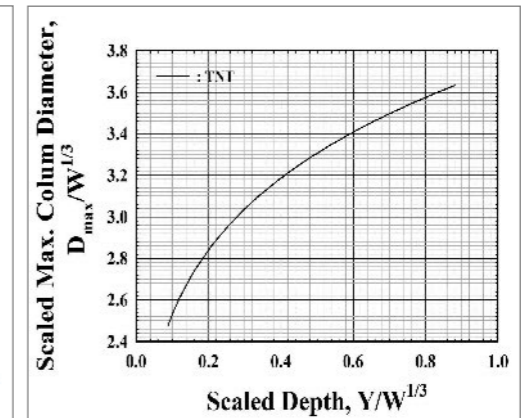
$$D_{max}/W^{1/3} = \text{scaled maximum column diameter (m/kg}^{1/3}\text{)}$$

$$S_{max}/W^{1/3} = \text{scaled maximum smoke crown diameter (m/kg}^{1/3}\text{)}$$

$$Y = \text{Charge Depth (m)}$$



〈Figure Appendix II-1-9〉 Maximum jet height vs. scaled depth for TNT



〈Figure Appendix II-1-10〉 Max. column diameter vs. Scaled depth

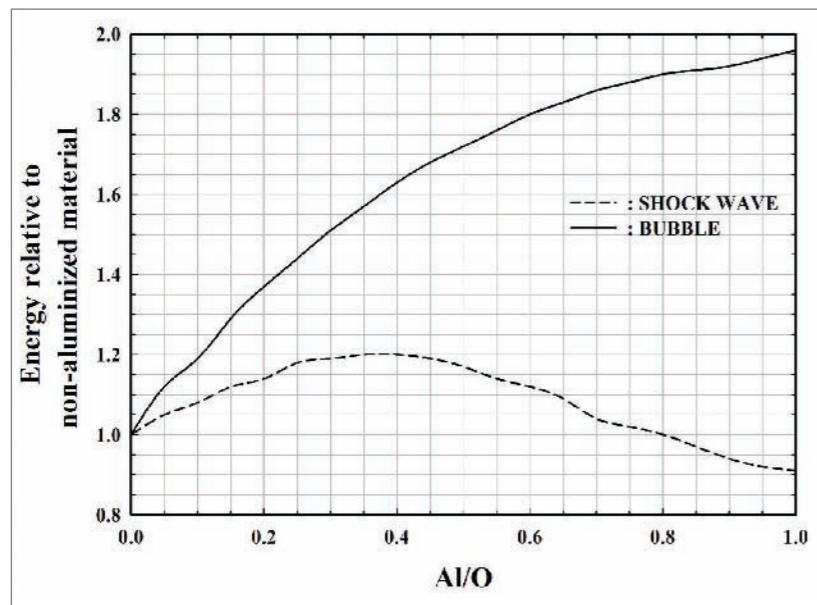
For example, by applying the graph on 〈Figure Appendix II-1-9〉, the maximum height of the water jet from an underwater explosion of a TNT charge of 250kg at a depth of 6m can be calculated in the following order:

- (1) $W=250\text{kg}$, $W^{1/4}=3.98$, $W^{1/3}=6.30$
- (2) $Y=6\text{m}$, $Y/W^{1/4}=6/3.98=1.51$, $Y/W^{1/3}=6/6.30=0.95$
- (3) In \langle Figure Appendix II-1-9 \rangle , $H_{\text{max}}/W^{1/3}=13$ at $Y/W^{1/5}=1.51$
- (4) $H_{\text{max}}=13 \times W^{1/3}=13 \times 6.30= 82$ meters

The column diameter calculation as shown in \langle Figure Appendix II-1-10 \rangle also uses the same method as above.

4) Underwater Explosion Performance of Aluminized Explosives⁵⁾

Non-ideal explosives containing a large amount of aluminum show dramatically increased bubble energy as their content increases, as shown in \langle Figure Appendix II-1-11 \rangle . It is usual to adjust the amount of aluminum in order to obtain the optimum ratio of the shockwave energy to the bubble energy according to their specific purposes. Most explosives for underwater weapon systems are aluminized explosives because bubble energy is more effective in destroying targets than shockwave energy.



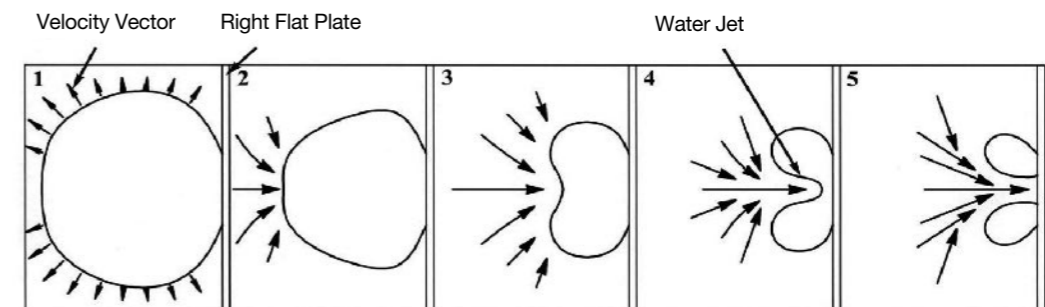
\langle Figure Appendix II-1-11 \rangle The effect of aluminum on underwater explosion properties

5) J. E. Shepherd, "Interface Effects in Underwater Explosions", AD-A201 814, December 1988.

When CHNO explosive containing aluminum is detonated underwater, it dissociates into elements such as C, H, N, O, Al almost instantly, and subsequently these elements undergo exothermic chemical reactions to form aluminum oxide(Al_2O_3), H_2O , H_2 , CO , CO_2 , and C(graphite) in a few micro-seconds. These high-temperature, high-pressure gaseous products push water in the radial direction to form a gas bubble, which expands and contracts as time continues.

2. Interaction between Rigid Wall and Gas Bubble⁶⁾

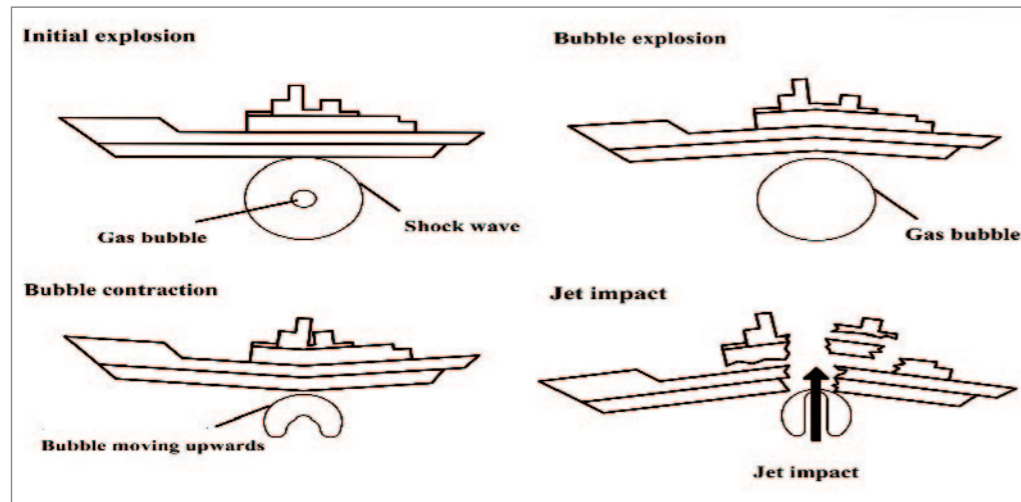
The descriptions on the gas bubble from underwater explosion hold only for deep underwater explosions where boundary conditions can be neglected. If there are free surface, seabed surface, or rigid wall located near the origin of explosion, the gas bubble behaves in a different manner. As shown in \langle Figure Appendix II-2-1 \rangle , when a bubble contracts near a rigid wall, the speed of the water is the highest on the opposite side of the wall and slowed down as it is closer to the wall, since the wall hampers free flow of water near it. Therefore, the bubble collapses toward the wall due to attraction, which results in the water jet effect on the opposite side of the wall. As the water jet develops, it applies a strong jet impact on the wall. After the water jet, the remaining bubble is deformed into a toroidal shape and gradually vanished. The collapsing procedure is heavily influenced by the size and oscillation period of the bubble, standoff from wall, gravity, and relative curvature of the wall and bubble.



\langle Figure Appendix II-2-1 \rangle Bubble collapse and formation of water jet

6) Julius W. Enig, "Underwater Explosion Bubble Dynamics", AD-A201 814, December 1988.

To facilitate the understanding of the sinking of ROKS Cheonan, the devastating effects of a gas bubble formed by an underwater explosion below hull will be explained with <Figure Appendix II-2-2>.

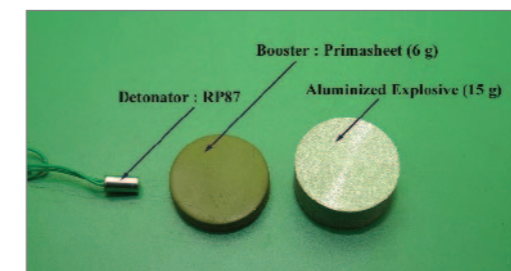


<Figure Appendix II-2-2> Physical effects of bubble formed below hull as time elapses

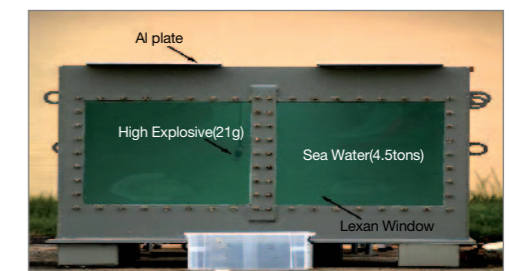
As an explosive charge is detonated below hull, shockwave is generated, and impacts the hull after propagating in water at a very high speed. Although the peak pressure of the shockwave is very high initially, it gets attenuated very rapidly as the shockwave propagates in water. Moreover, since the shockwave travels outward spherically, the actual impact on the hull is not severe. For these reasons, the damage inflicted by the shockwave is known to be insignificant, such as malfunctioning of on-board power and communication systems, and light damage of the body. After the shockwave passes, the bubble is formed slowly, and the pressure inside the bubble is relatively low compared to that of the shockwave. As the bubble expands, the hull is deformed into a reverse V-shape under the force exerting upward. Then, the bubble starts to contract, pulling the hull downward to produce a V-shape deformation. As the contraction continues, the bubble collapses and the high speed water jet starts to be formed in the lower part of the bubble. As the water jet gets larger, it produces a heavy impact on the hull, and eventually breaks the hull. Since the water jet impact is much more effective than the shockwave, most countries employ aluminized explosives for non-contact underwater weapon systems.

3. Small-scale UNDEX Experiments

In order to demonstrate the formation of a bubble and analyze the chemical components of the white substance adsorbed on the fractured surface and the stack of ROKS Cheonan, a small-scale underwater explosion experiment was conducted. A water tank (2m × 1.5m × 1.5m) was filled with 4.5 tons of water, and an aluminized explosive of 15g was detonated in the aquarium by using 6g of a booster and a RP87 detonator, as shown in <Figure Appendix II-3-1>.



<Figure Appendix II-3-1> Explosive train used in the experiment



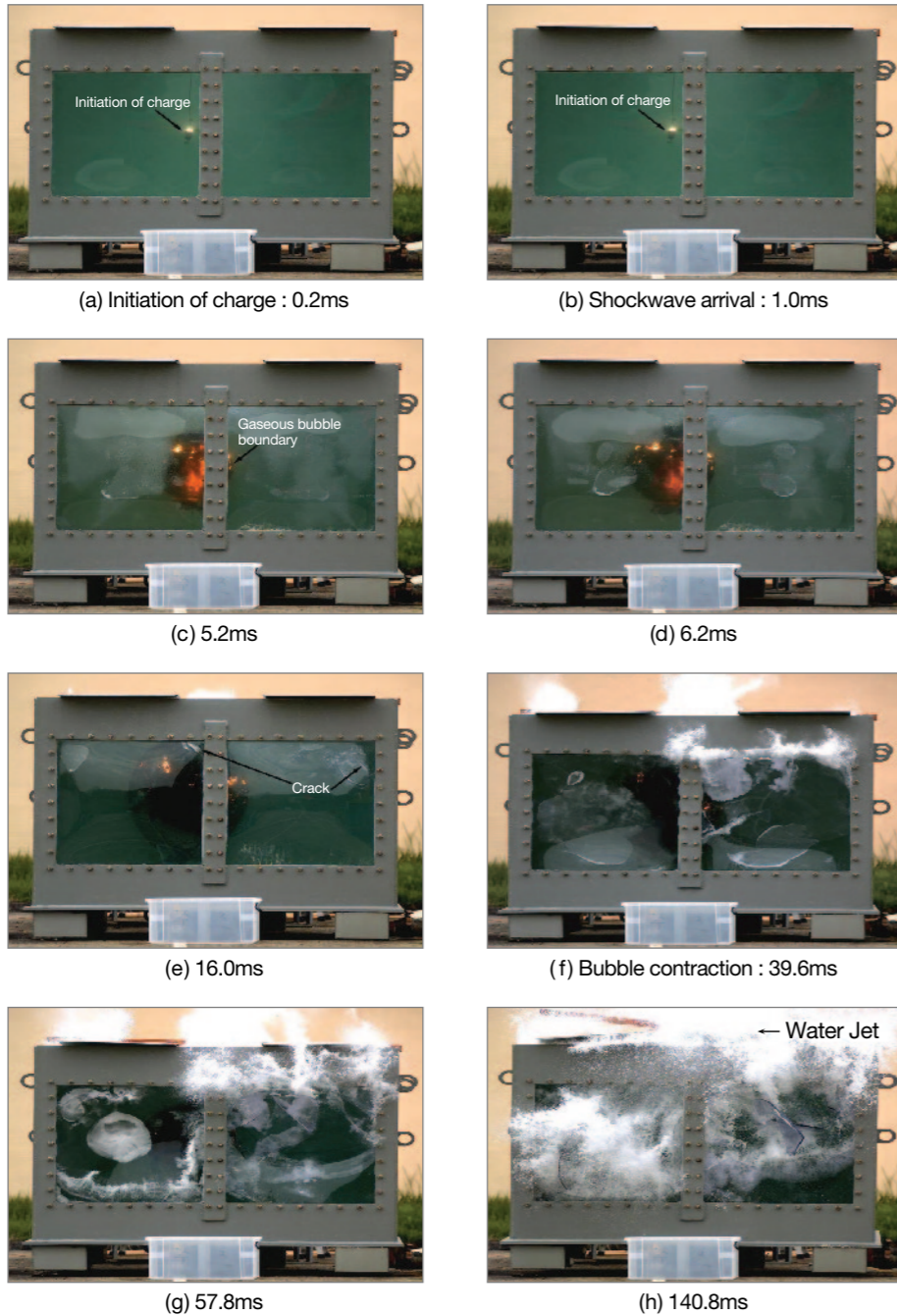
<Figure Appendix II-3-2> Small water tank used in the UNDEX test

To obtain the adsorbed materials, the team placed 2 layers of 4 aluminum plates on top of the tank, and fixed them with bolts to prevent the aluminum plates from being thrown by the water column. Also, 2 polycarbonate windows were installed for high-speed image as shown in <Figure Appendix II-3-2>. The writing speed of the high-speed camera was set 5,000fps(frames per second).

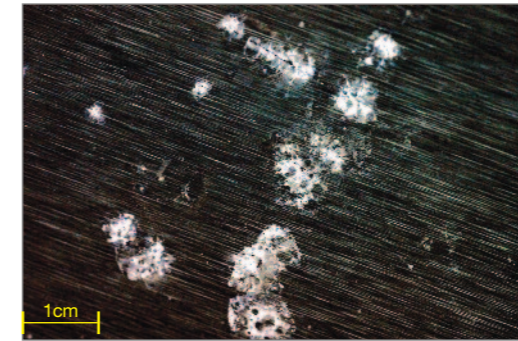
<Figure Appendix II-3-3> are pictures of the selected frames taken from the high-speed photograph record, showing the development of the bubbles formed by the underwater explosion. In <Figure Appendix II-3-3> (a), the charge produces strong flash at 0.2ms after initiation. In (b), the window becomes opaque by the impact of the shockwave to the window at 1ms. In(c) and (d), the heat is released inside the high-temperature and high-pressure bubble. The bubble expands and begins to apply pressure against the window. In (e), the window starts to break. The window continues to break until the bubble reaches its maximum radius. In (f), the bubble starts to contract. In (g), as the contraction continues, the left window experiences a strong attraction force towards the contracting bubble. In (h), the window breaks completely.

In this small-scale underwater explosion test, white substance adsorbed on the alu-

minimum plate was obtained as shown in <Figure Appendix II-3-4>. Through detailed analysis and comparison of the white substance, an important clue for the sinking of ROKS Cheonan was found.



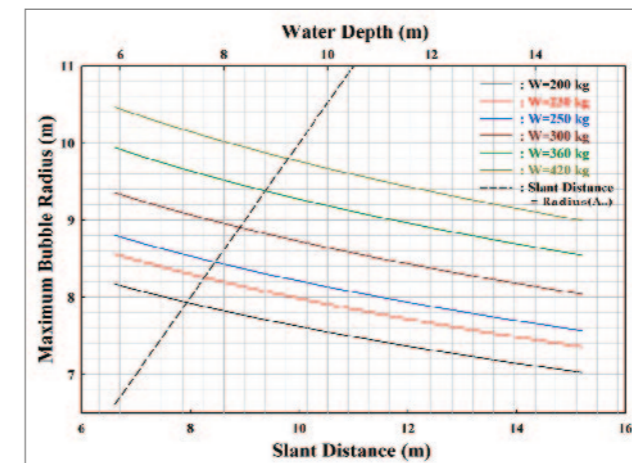
<Figure Appendix II-3-3> Images obtained through the experiment(5,000 frames/sec)



<Figure Appendix II-3-4> White substance obtained from the small-scale UNDEX experiment

4. Conditions for the Maximum Bubble Effects

To determine the type of the weapon system, a depth of the explosion, the TNT equivalent weight of the explosive from surfaces of the salvaged hull, and theoretical and empirical formulas for an underwater explosion were applied. <Figure Appendix II-4-1> summarizes the most plausible explosion conditions chosen under the assumption that bubble jet caused the break. Since the bubble jet is formed only in the presence of a rigid wall near the origin of the explosion, the maximum effect occurs when the maximum bubble radius(A_m) and the slant distance between the keel and the origin are approximately the same. Hence the maximum bubble jet effect is obtained in the range of charge size(200~360kg TNT equivalent) and depth(6~9m) near the dashed line in <Figure Appendix II-4-1>.

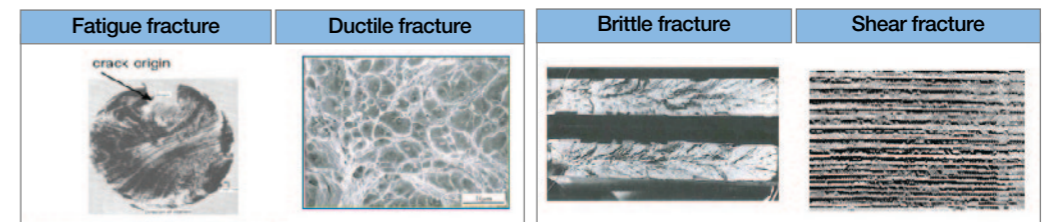


<Figure Appendix II-4-1> Maximum bubble radius vs. slant distance

For instance, when 250kg of TNT equivalent and 6m depth are applied to the equation (5), which is used for a calculation under the free sea surface environment, the projected value of the maximum height of the water jet is computed as approximately 82m.

Appendix III. Analysis Result on Direction and Location of the Explosion

In order to analyze explosion effects with varying charge size, the direction of the explosion with respect to the ship needs to be determined first. For this end, the breakplane of the hull, the most assured evidence, was analyzed. The types of damage on the breakplane were visually investigated and analyzed. From this, it was determined whether the fracture includes fatigue, ductile, brittle or shear fracture. Based on this observation, the direction and location of the explosion were estimated.



〈Figure Appendix III-1〉 Types of fractures

Fatigue fracture stems from repeated stresses over a long period of time, and contains a beach mark from the crack origin. Ductile fracture occurs when the stress is applied relatively slowly, and is accompanied by a large plastic deformation. The cross section is relatively rough and contains many dimples. Brittle fracture occurs with a small plastic deformation when the stress is applied rapidly. The section is relatively smooth and contains chevron marks. Shear fracture results from high stress applied rapidly in shear direction, and it shows no chevron marks, dimples, or beach marks. In the shear fracture, fracture occurs in the direction of the stress.

1. On-site Investigation and Sample Collection

The first on-site investigation was conducted on April 30, and the breakplane of the stern hull bottom was observed. As shown in <Figure Appendix III-1-1>, samples of approximately 15cm × 15cm size were collected from three locations at the breakplane of the stern hull bottom. The second on-site investigation was conducted on May 4, to check the probable direction of fracture on the bottom of the stern hull, and to observe the breakplane on flank of the stern hull as well as on the bottom and flank of the bow hull. On May 10, the third on-site investigation was conducted in order to check the direction of fracture on the bottom and flank of the bow, and breakplane of main deck of the bow and stern was observed.

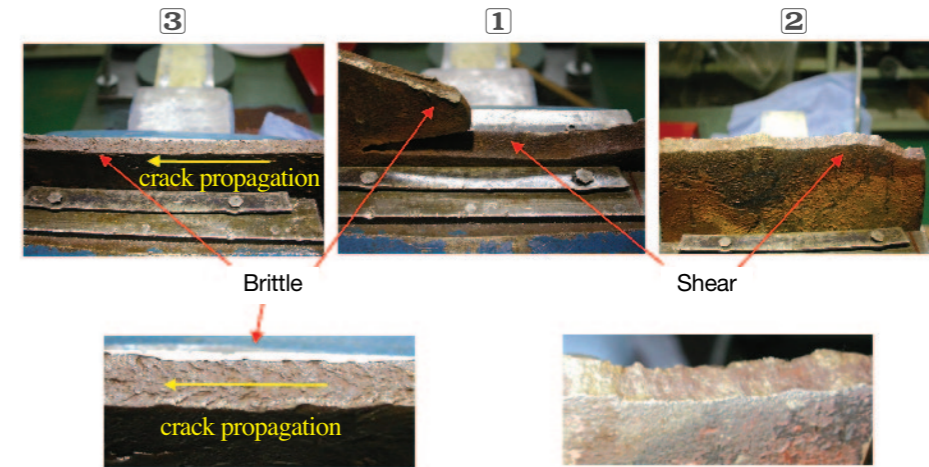


<Figure Appendix III-1-1> Sample collection locations at breakplane

2. Results for Breakplane Analysis

1) Estimation of Fracture Type

All the fractured surfaces of the samples, as shown in <Figure Appendix III-2-1>, were identified to be shear and brittle fractures with no signs of ductile or fatigue fracture. Sample #2 shows shear fracture patterns and sample #3 shows a typical brittle fracture, whereas sample #1 contains a mixture of the two.



<Figure Appendix III-2-1> Fracture surfaces of collected samples

2) Estimation of Fracture Direction

Additional visual observation was made on May 4, and it was confirmed that the pattern showed shear fracture between sample locations #1 and #2 and brittle fracture between sample locations #1 and #3 as shown on <Figure Appendix III-2-2>.

Therefore, it was estimated that one third of breakplane on the port side of the stern hull underwent shear fracture caused by instantaneous external force, and the rest of bottom part of the stern hull suffered brittle fracture caused by tensile force. And the origin of crack was estimated to be near sample location #1.



<Figure Appendix III-2-2> The pattern of fracture on the stern

As shown in <Figure Appendix III-2-3>, it was confirmed that in the fractured surface of the stern part, shear fracture(highlighted in red) occurred in the estimated region of direct impact, and that brittle fracture(highlighted in blue) occurred starting where shear fracture ends, towards the starboard side. In addition, all of the three fractures on the port side, which was rolled up into a U-shape, also showed shear fracture patterns.



<Figure Appendix III-2-3> Overall fracture pattern of the stern part

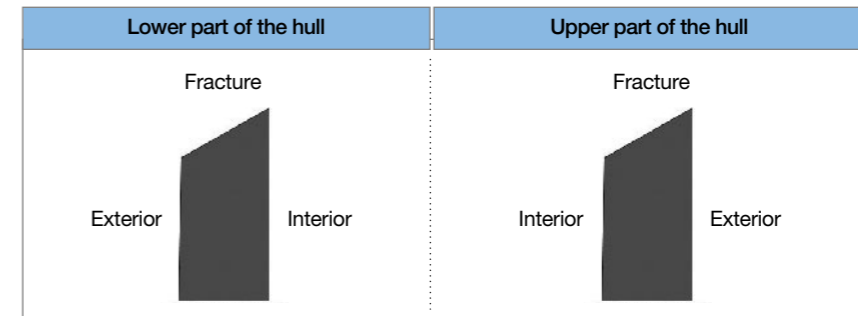
The JIG also conducted visual observation for the fractured surface of the bow section, and confirmed that the overall pattern is similar to that of the stern section. Both shear fracture and brittle fracture were observed partially near the estimated origin of impact on the port side, and it was assessed that this condition was due to the influence of internal structures on the fracture surface in a complicated manner.

3) Observation Results for Fracture Direction(Stern and Bow)

The brittle fracture patterns were observed in the vicinity of the keel for both the bow and stern part, and the shear fracture patterns were shown in all the rest. The estimated origin of the brittle fracture was the lower-left part of the port hull(near sample location #1). In the lower part of the port side and starboard side of both the bow and stern that show the shear fracture patterns, the overall cross section was slanted from the vertical direction and lifted higher towards the interior of the hull as shown in <Figure Appendix III-2-4>(the di-

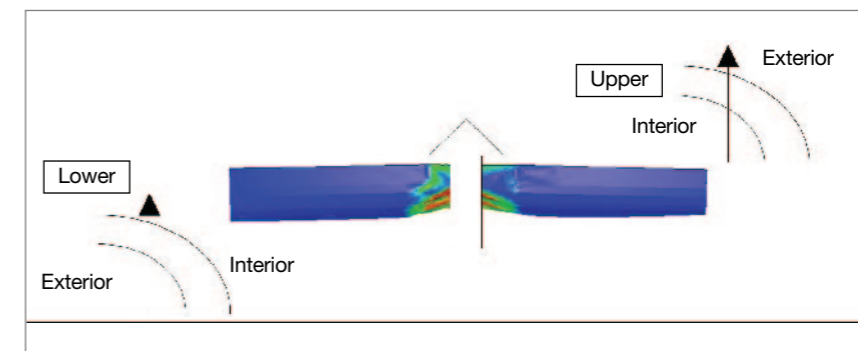
agram on the left) at every location.

For the port and starboard sides of the upper main deck of both the bow and stern, the overall section was also slanted; however, the direction was reversed and oriented higher towards the exterior of the hull as can be seen in <figure Appendix III-2-4>(the diagram on the right) at every location.



<Figure Appendix III-2-4> Shape of fracture on the hull

The situation that could have caused the aforementioned section shapes, as shown in <Figure Appendix III-2-5>, was estimated to happen when a large plastic deformation occurs first to curve the outer structure of the ship, followed by a shear fracture caused by a strong, uni-directional external force(presumably water jet).

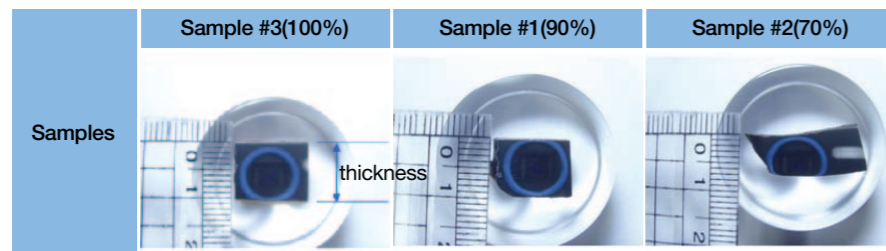


<Figure Appendix III-2-5> Analysis of cutting shape of upper and lower hull

3. Microstructure Analysis of Collected Samples

1) Thickness Comparison of Collected Samples

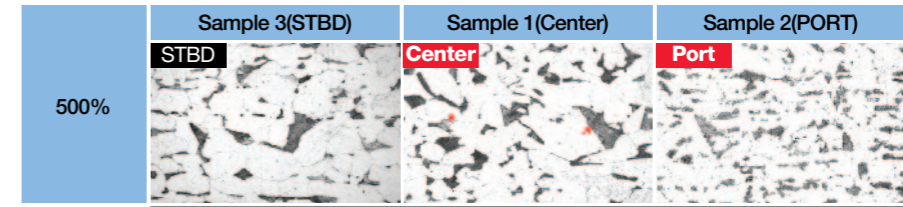
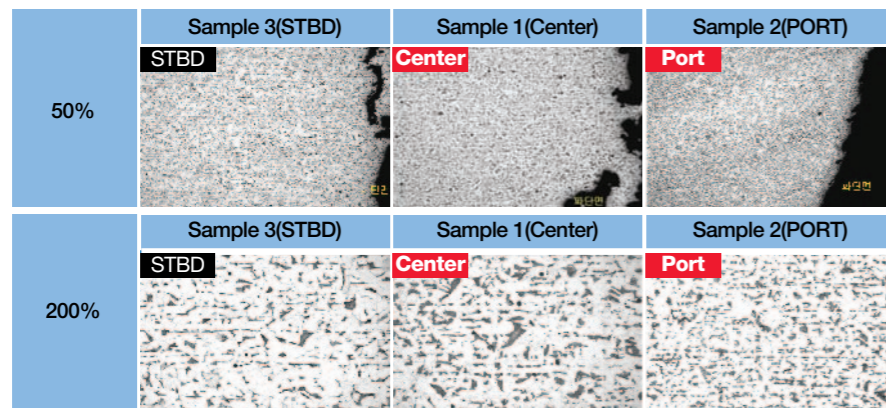
From the measurement of the thickness of collected samples, sample 2 which was estimated to be near the origin of explosion showed to be 30% less thick than sample 3 at starboard side, while sample 1 showed 10% less compared to sample 3, as shown in <Figure Appendix III -3-1> below.



<Figure Appendix III-3-1> Thickness measurement of collected samples

This confirmed the assessment mentioned earlier that a plastic deformation with substantially large curvature occurred at the port side bottom before fracture.

2) Comparison of Microstructures



<Figure Appendix III-3-2> Microstructures of collected samples

The observations of the microstructures of each sample and the results are shown in the <Figure Appendix III-3-2>.

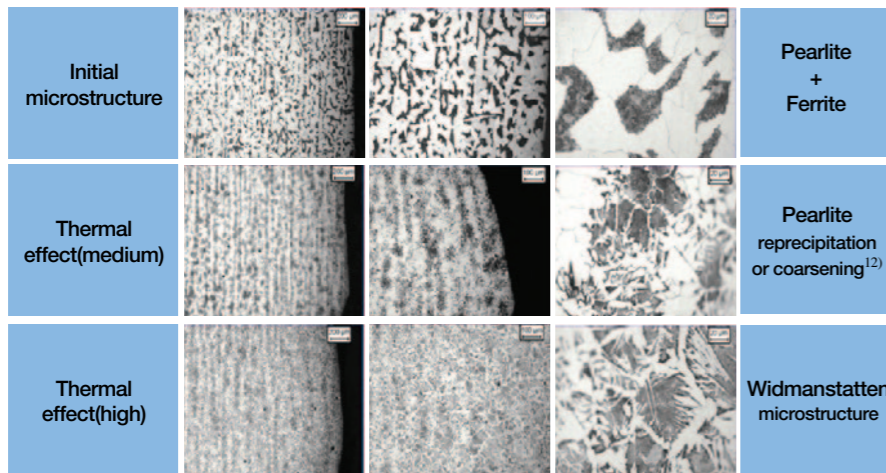
For the 50× magnified images, all the samples showed a rolling structure⁷⁾ with horizontal stripes⁸⁾; however, sample 2 from portside showed denser stripes than the initial structure due to about 30% thickness reduction and longitudinal extension.

For the 200× magnified images, the sample 2 showed the stripes spaced closer and thinned out compared to sample 3 collected from starboard side, and showed typical pearlite + ferrite⁹⁾ microstructure. The black parts were pearlite structure. If there were a heat deformation on the portside, as shown in <Figure Appendix III-3-3>, rolling stripe melting due to pearlite coarsening should be observed; however, since such phenomena were absent on the samples, it was confirmed that there had been no heat over 723℃. This can be a basis in proving the cause as a non-contact external explosion.

For the 500× magnified images, the sample 2 showed grain refinement¹⁰⁾ due to relatively greater plastic deformation stemming from thickness reduction and longitudinal extension.

Micro hardness for samples 2 and 3 was Hv=163 and Hv=146 respectively, and it was assessed that the hardness of sample 2 would become higher due to the significant strain hardening¹¹⁾ of the sample on the portside.

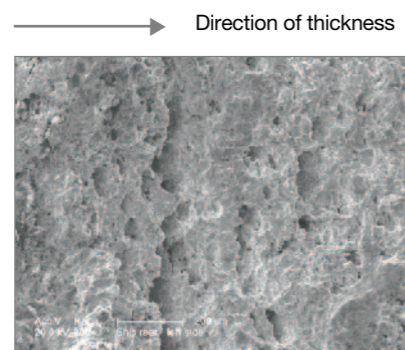
7) Rolling structure: Metallic formation with more thorough crystalline particles. This structure is produced by the pressure created from the metallic material being inserted between two spinning rollers.
 8) Rolling stripe: The marks arranged in stratified fashion as a result of rolling process.
 9) Pearlite and Ferrite: A microscopic structure from during the process of steel that has approximately 0.25% less carbon freezing after being melted in a high temperature.
 10) Grain refinement: The size reduction of certain crystalline substances due to external pressure or heat.
 11) Strain hardening: An increased hardness of a metal through a deformation or method of processing.



〈Figure Appendix III-3-3〉 Typical microstructure change due to heat influence(example)

3) Microstructure Analysis on the Fractured Surface of the Samples

As the microstructure of the sample 2 from portside was observed, numerous cavities grown perpendicular to thickness appeared as shown in 〈Figure Appendix III-3-4〉, which indicated a strong tensile force having been applied in the direction of thickness. This tensile force was caused to be from the tensile wave due to the interaction between shockwave in the direction of thickness and rarefaction wave¹³⁾ on the opposite free surface side of the impact. Therefore, this was another basis that could prove the strong impact upon the portside bottom.



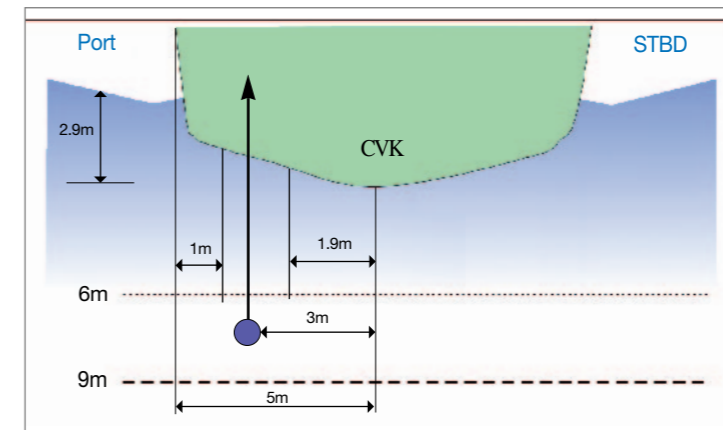
〈Figure Appendix III-3-4〉 A microstructure of fractured surface

12) Pearlite coarsening: Crystalline substances getting bigger than original size. Reprecipitation: Certain crystalline substances are recreated.

13) Rarefaction wave: A phenomenon in which shockwave is propagated to the opposite side after it encounters free surface and slows down during its progression.

4. Estimation on Location and Direction of the Explosion

The analysis on the breakplane of ROKS Cheonan revealed that an upward plastic deformation with large curvature due to a strong explosion from the portside bottom occurred(hogging), and then, a strong external force, presumably water jet, caused shear fracture which began at 1.9m left of the CVK. Thus, given that the hull is 5m in half breadth of the port, it could be estimated that an explosion might have occurred between 1.9~5m left of the CVK. The possible location for a torpedo strike could be estimated to be 3m, which is the center of 1.9~4m range left of the bottom CVK(See 〈Figure Appendix III-4-1〉).



〈Figure Appendix III-4-1〉 Possible range of torpedo explosion

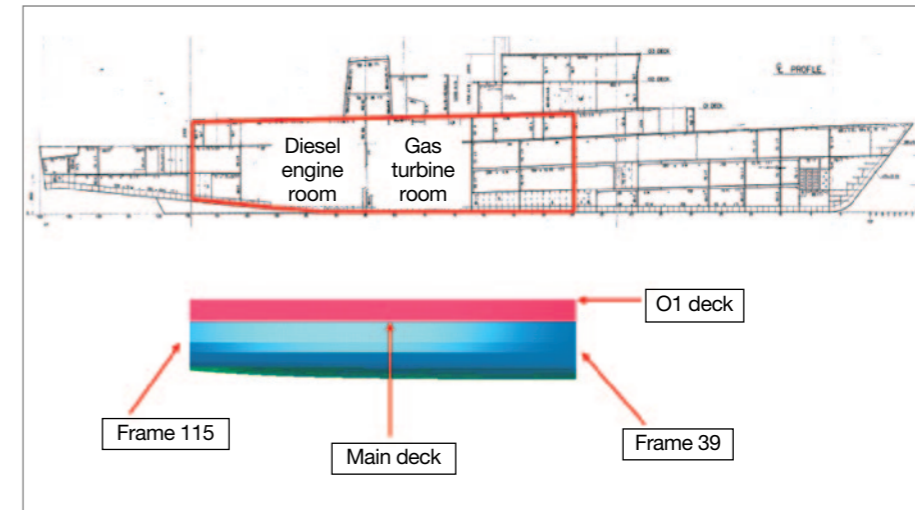
Appendix IV. Analysis Result on Charge Size and Depth

Based on the location of explosion and the direction of external force derived from the earlier mentioned analysis of breakplane, simulations were conducted in order to estimate the charge size and depth similar to the explosion that occurred in the ROKS Cheonan incident. Explosion Analysis Team utilized a simplified model(localized area and simplified ship modeling) in order to derive the range of probable explosion types in a short period time. Based on this result, Ship Structure Management Team conducted a detailed analysis using full modeling of the entire ship. The result from the simplified model is presented here.

1. Numerical Model

Though the entire ROKS Cheonan should have been modeled in 3D for accurate results, a portion centered around the gas turbine room, which was lost, was covered in this simulation, and only the local damage of this portion was analyzed. This was because plausible explosion types had to be estimated within a short time, and simulations on the entire ROKS Cheonan for all possible loads(shockwave, bubble pressure, whipping effect, and water jet) were assigned to Ship Structural Management Team. Probable explosion types(charge sizes and locations) were derived from numerical simulations using this simplified model. Therefore, this analysis was expected not to include detailed whipping effects, with a 3D modeling confined to the region between Frame 35 and Frame 119 of ROKS Cheonan that included the gas turbine room and the diesel engine room as shown on <Figure Appendix IV-1-1>.

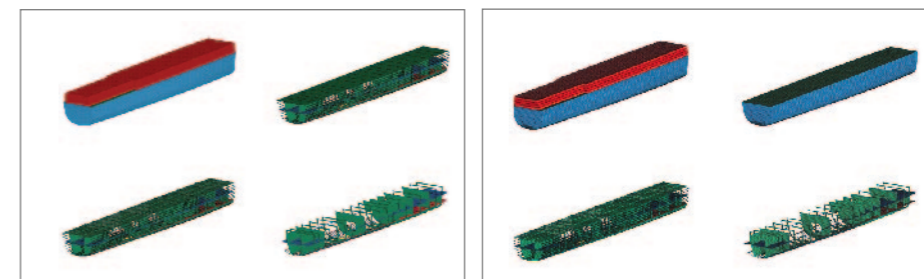
For the simulation, LS-DYNA™ code was used, a commercial code developed in the United States. Many government and civilian labs of ROK as well as the US, Japan, PRC, and EU countries use this code to analyze high pressure hydrodynamic phenomena such as explosions and collisions, and the credibility of this code is widely recognized. This code had also been used in Korean labs for design and performance prediction of various warheads.



<Figure Appendix IV-1-1> Simulation range for explosive analysis

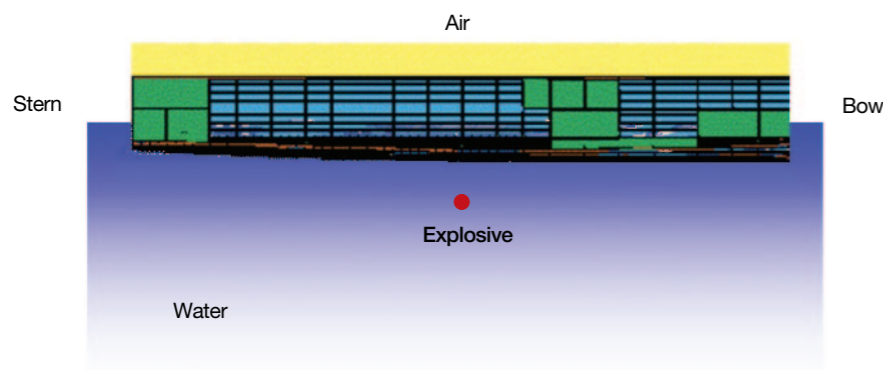
Prior to the simulation, a 3D geometrical modeling should be conducted first, which usually takes a lot of time and manpower. This is because the 3D modeling itself is a time-consuming process, and normally several modifications to the 3D model are needed due to errors and inaccurate results in calculations.

<Figure Appendix IV-1-2> shows a ship configuration(45.6m) modeled from Frame 39 to Frame 115 of ROKS Cheonan, and <Figure Appendix IV-1-3> shows the configurations with approximately 300 × 300mm meshes superimposed on the geometrical model to enable numerical simulations. I-DEASTM code, which is used widely, was used in the modeling process.



<Figure Appendix IV-1-2> Modeling shape

<Figure Appendix IV-1-3> Mesh shape



〈Figure Appendix IV-1-4〉 Initial analysis model

2. Conditions for Numerical Simulation

In order to derive probable explosion types that caused the ROKS Cheonan incident, simulation conditions were first determined based on simulation results of US Team, break-plane analysis, and analysis of probable hostile weapon systems.

Explosive charge weights of 45~500kg TNT equivalent and depths of 6~13m were selected considering a detection capability of weapon systems and assuming a non-contact explosion. Three meters to the portside from the center of the gas turbine room was selected as the widthwise location of the explosion from the results of the breakplane analysis. Frame 71, 2.4m to the bow from the center of the gas turbine room, and Frame 75, the center of the gas turbine room, were selected as lengthwise locations of the explosion. Frame 71 was selected because the bulkhead of the gas turbine room at the breakplane and CVK of bow part experienced deformation greater than that of the stern part. Frame 75 was selected in order to exclude explosion types with smaller explosive charge weights that inflict less deformation than the actual damage, by performing calculations at a location where the greatest deformation of the gas turbine room is produced. The simulation was conducted from Frame 75 to derive probable explosion types, and then additional simulation was carried out at Frame 71. A final range of explosion types was derived by comparing and analyzing the two results. 〈Table Appendix IV-2-1〉 shows selected conditions for the simulation.

Charge weight (kg, TNT equivalent)	Frame location	Depth of explosion(m)
45	75	6
200	75	6, 7, 8
250	75	6, 7, 8, 9, 12
300	71, 75	6, 7, 8, 9, 11
360	71, 75	6, 7, 8, 9, 11
420	71, 75	6, 9, 12
500	71, 75	10, 11, 12, 13

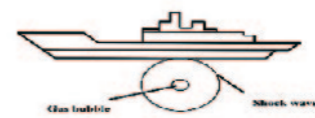

〈Table Appendix IV-2-1〉 Simulation conditions(3m to port)

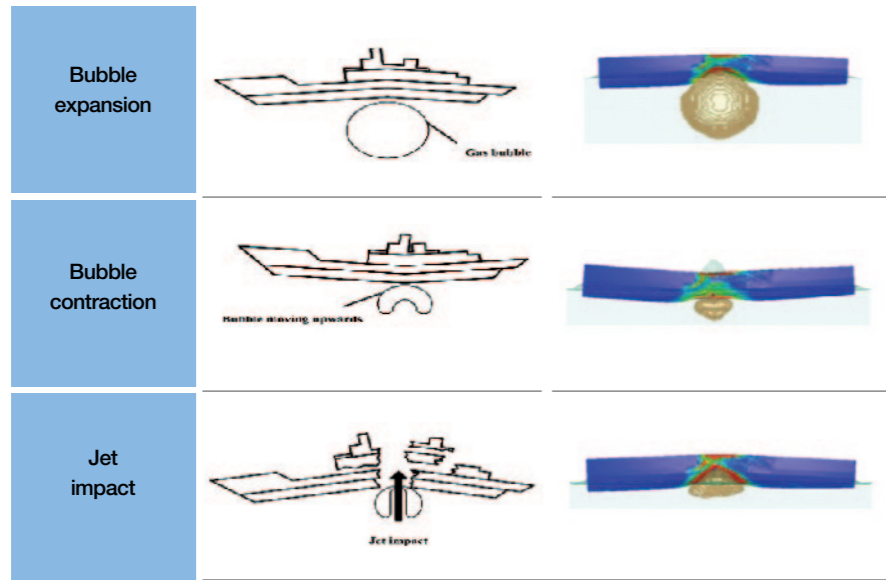
For validation of the simulation results, computation results of shockwave pressure on different distances from a point of underwater explosion were compared with results from well-known empirical equations before performing numerical simulations on each model. 〈Table Appendix IV-2-2〉 summarizes the results. As shown in the table, calculated values and empirical values were consistent, and they fell under 5% difference.

Charge size (kg, TNT)	Measured radius(m)	Empirical value(MPa)	Calculated value(MPa)	Error(%)
250	3	130.14	135.39	4.0
	6	50.25	52.97	5.4
	9	31.66	33.20	4.9

〈Table Appendix IV-2-2〉 Comparison of shockwave pressure

Secondly, the credibility of the results was ensured by comparing the bubble behavior appeared on the simulation with the actual behavior shown in 〈Figure Appendix II-1-1〉. 〈Figure Appendix IV-2-1〉 compares the two cases.

Bubble behavior	Actual	Simulation
Initial explosion		



〈Figure Appendix IV-2-1〉 Comparison of bubble behavior

3. Criteria for Selecting Probable Explosion Types

The team established three criteria and selected explosion types that satisfied all three as probable explosion types.

The explosion types were selected on the basis of the extent of hull bottom damage at the gas turbine room which is visible on both port and starboard sides, and the way two damaged parts engage with each other. This was because the entire gas turbine room of ROKS Cheonan was lost.

Since this simulation model did not include the entire ship as well as interior components, the calculated deformation would have been greater than the actual deformation. Therefore, the CVK deformation at the sides of the stern part, where many of the structures were arranged transversely, was selected as a criterion. On the actual bulkhead of the break-plane, the CVK deformation was smaller at the stern part than at the bow part. The deformation length(actual value: 3,580mm) was selected as a criterion of the CVK deformation. CVK deformation length was set to one shown in 〈Figure Appendix IV-3-1〉. From the simulation result of each case, the deformation length within 1~1.2 times of the actual de-

formation was selected to meet the criterion. This, as mentioned earlier, was because the simulation would have yielded a greater deformation than the actual value due to the simplified modeling.

Lastly, the shape of deformation/fracture at the stern breakplane bulkhead was included. 〈Figure Appendix IV-3-1〉 shows all three criteria.

Criteria	ROKS Cheonan	Simulation, example
① Extent of hull bottom damage		
② Deformation/fracture at the stern failure-section bulkhead		
③ CVK deformation length toward stern from failure-section		

〈Figure Appendix IV-3-1〉 Three comparison criteria

4. Simulation Result

Simulations for charge weight of 230kg TNT equivalent or below, at Frame 75, 3m to the port were conducted and compared with the actual damage observed on ROKS Cheonan. As a result, it was concluded that the explosion caused by charge weight of 230kg TNT equivalent and below was unlikely to have occurred. For the charge weight of 250kg TNT equivalent, the explosion type to partially match the actual damage was estimated to be at

a depth of 6m, and for 300kg of TNT equivalent, the possible explosion type was at a depth of 7m. The result of the simulation at Frames 71 and 75 at 3m to the portside from the center and with 360kg TNT equivalent, a depth of 7~9m was selected to be the possible explosion types.

Therefore, from numerical simulations of various conditions of different charge sizes and standoffs(6~13m), and by using 3m to portside as location range of explosion from the breakplane analysis, the explosion types showing similar damage pattern as the actual were derived as shown in <Table Appendix IV-4-1>.

Explosive wt.(TNT, kg)	Depth(m)
250	6
300	7
	7
360	8
	9

<Table Appendix IV-4-1> Summary of simulation results

Appendix V. Analysis Result on Adhered Materials

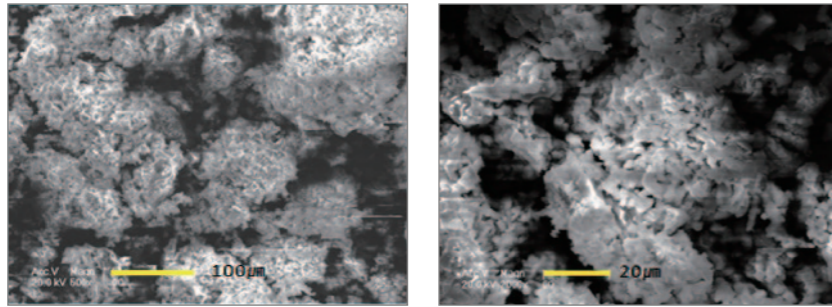
In order to analyze the explosion pattern, the explosive weight and location of explosion were estimated so far. In this section, a large amount of adhered material found on ROKS Cheonan was analyzed for confirming possible weapon system that might have caused such explosion.

When the stern of ROKS Cheonan arrived at 2nd Fleet(Pyeongtaek), the initial visual inspection was made on April 18. While observing the fracture on the stern, a large quantity of white powder was found adsorbed on crumbled aluminum panels of the upper deck on the portside. In addition, the same kind of material was observed around the fracture surface on the upper deck, as well as on the shell plating of the stern. Such adhered material was found not only on aluminum panels but also on power cables composed of non-aluminum material. A five-step analysis was performed on the adhered material: the first analysis was preliminary to understanding the characteristics of white powder found during the initial observation, and the second and third analyses were detailed examinations on the adhered material found on the stern and bow. The fourth analysis was conducted to investigate whether the adhered material from the recovered propulsion parts of the torpedo(conclusive evidence) was the same as the material adsorbed on the bow and stern. The final analysis was conducted with the explosion products from the small-scale underwater explosion experiment in order to verify that the adhered material found inside ROKS Cheonan was a product of aluminized underwater explosives.

1. First Analysis

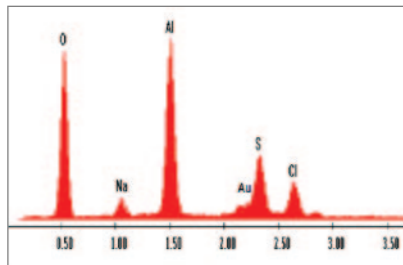
The apparatuses employed in the composition analysis were SEM(Scanning Electron Microscopy; Philips XL30), EDS(Energy Dispersive Spectrometer; Philips EDAX) and XRD(X-ray Diffraction; Bruker D8 Discover).

The SEM images of the adhered material are shown in <Figure Appendix V-1-1>. Fine particles were agglomerated as if melted.

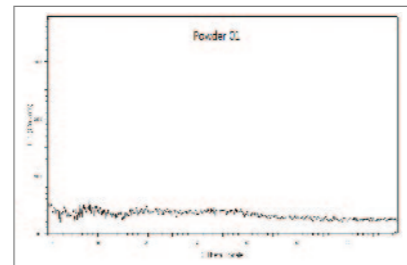


〈Figure Appendix V-1-1〉 SEM Images

For EDS analysis, electrons of an atom are ejected upon irradiation of an electron beam, and subsequently the hole is filled with other electrons from higher shells which accompany energy release. Since the released energy is different for each element, the elements composing of a material can be identified. As presented in 〈Figure Appendix V-1-2〉, the EDS results show that the adsorbed material consisted of oxygen, sodium, aluminum, sulfur, and chlorine(The Au(gold) peak was observed due to the gold plating on the sample necessary for the experiment). Based on the elemental composition, the adhered material was considered to be a mixture of oxides of aluminum(Al_xO_y), salt(NaCl), and sulfur or sulfur compounds.



〈Figure Appendix V-1-2〉 EDS result



〈Figure Appendix V-1-3〉 X-ray diffraction result

In XRD analysis, X-rays scattered from different atoms within the crystal mutually interfere with each other. If the incident X-ray is monochromatic, the scattered beams for each type of atom interfere to give strong diffraction patterns in a certain direction. The diffraction peak¹⁴⁾ depends on the distance between each lattice in the crystal, i.e. the size of

14) Diffraction peak: The display of the reinforcement interference of an x-ray. This display can be observed in certain angles when the x-ray is projected on the object and gets scattered by the object's crystal.

unit cell. Therefore, each crystal has its own X-ray diffraction peak, while amorphous material does not show one.

As shown in 〈Figure Appendix V-1-3〉, the adhered material did not show any noticeable X-ray diffraction peak, which means it contains mostly amorphous material, not crystalline ones. By combining the analysis results obtained from SEM, EDS, and XRD, the adhered material was agglomerates of fine particles, and mainly consisted of amorphous oxides of aluminum with a small portion of sulfur or sulfur compound along with salt.

Normally, the surface of pure aluminum undergoes oxidation in a very short time and becomes a thin layer(several nanometer) of amorphous aluminum oxide. Since this layer is quite dense and oxygen is unable to penetrate this layer, there ought to be no further oxidation inside this layer. However, when the aluminum is exposed to moisture, acids and bases for a long time, it forms white corrosion products. The major components of these white corrosion products are aluminum hydroxide($Al(OH)_3$, bayerite) along with boehmite($AlO(OH)$) and Al_2O_3 , all of which are known to be crystalline, rather than amorphous. On the contrary, the adhered white material found on the stern of ROKS Cheonan is white amorphous oxides of aluminum, which is assessed not to have experienced corrosion in a natural state.

2. Second Analysis(Material Adhered on the Stern)

Based on the first analysis results, samples were collected from five different locations on the stern on April 22, 2010 to perform more extensive analysis. Sample locations were near the center of the fracture plane, where a significant amount of the adhered powder was found, and included surfaces of different types of materials(aluminum and non-aluminum). The team also sampled from the 76mm naval gun barrel which was relatively far from the fracture plane.

Sample #	Location	Surface material
1	Aluminum angle bar in crew's mess kitchen	Aluminum alloy
2	Crew's mess kitchen wall(water fountain)	Aluminum alloy
3	Mesh cable of switch board in crew's mess kitchen	Non-Al alloy
4	Mesh cable above crew's mess kitchen	Non-Al alloy
5	76mm naval gun barrel	Iron

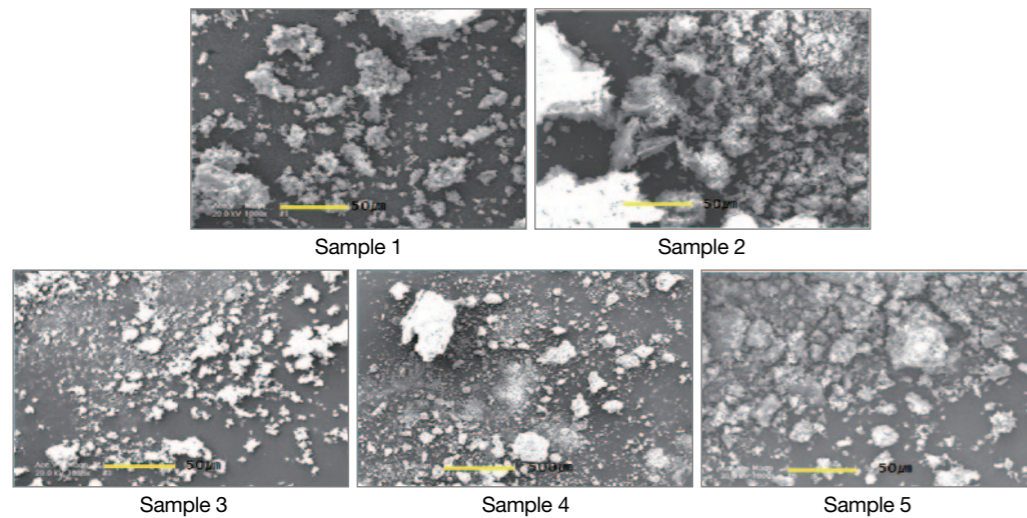
〈Table Appendix V-2-1〉 Sampling locations



〈Figure Appendix V-2-1〉 Sampling locations

Along with the instruments used in the first analysis, the second analysis utilized CHNS¹⁵-EA(CHNS - Elemental Analyzer, Thermo EA1112) and TGA(Thermal Gravity Analyzer, Mettler TA30).

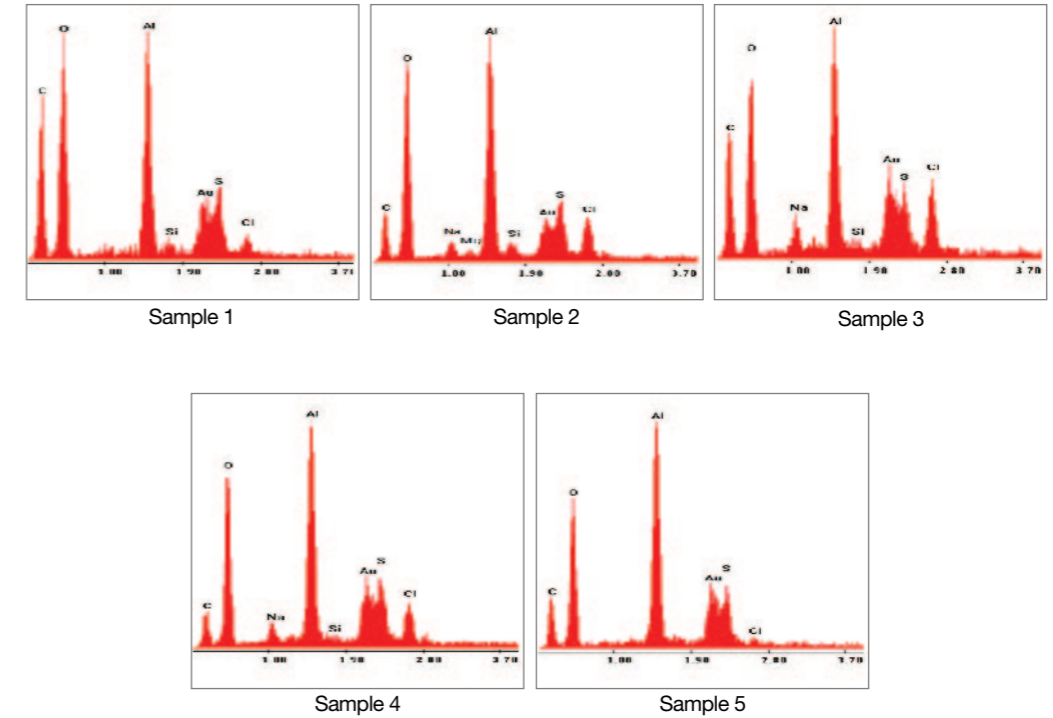
The SEM images of the collected samples showed agglomerates of fine particles, which were similar to those obtained in the first analysis(See 〈Figure Appendix V-2-2〉). In the EDS analysis, the detection range was increased to detect elements with low atomic weight, and consequently the carbon was detected.



〈Figure Appendix V-2-2〉 SEM images of the adhered material(stern)

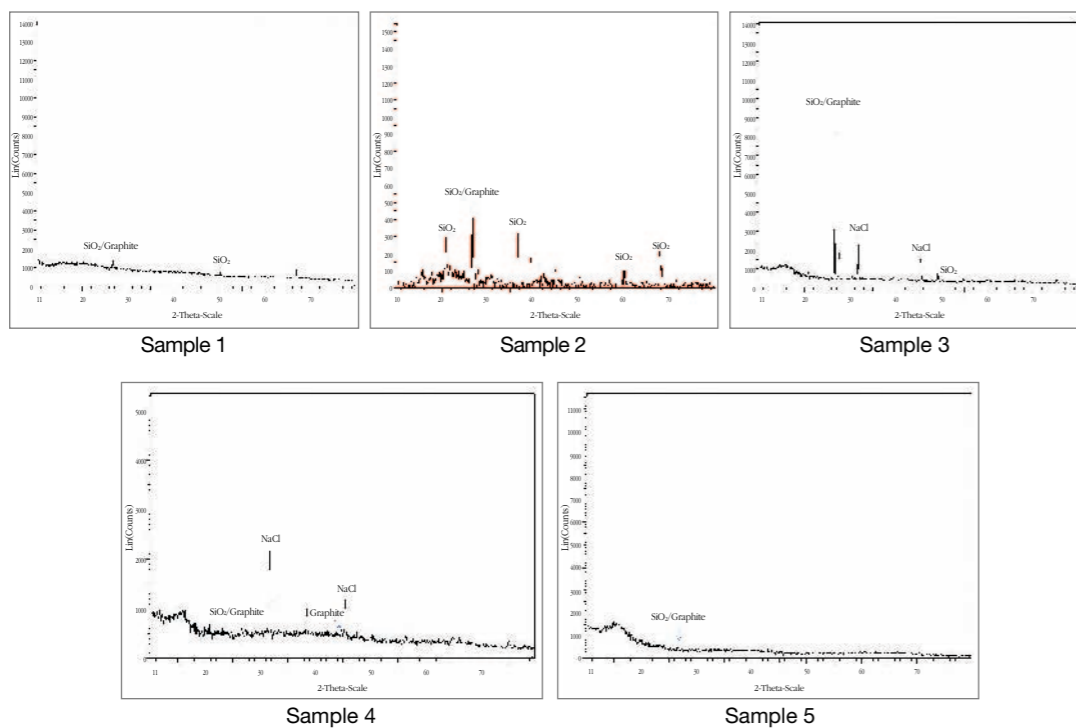
15) CHNS: Carbon Hydrogen Nitrogen Sulfur

As shown in 〈Figure Appendix V-2-3〉, all samples consisted of carbon, oxygen, sodium, magnesium, aluminum, silicon, sulfur, and chlorine. This result was similar to that of the first analysis. Considering the elemental composition, the adhered material consisted of oxides of aluminum(Al_xO_y), salts($NaCl$, $MgCl_2$, etc.), and sulfur or sulfur compounds.



〈Figure Appendix V-2-3〉 EDS results of the adhered material(stern)

The XRD results showed silicon dioxide(SiO_2), graphite, and salt($NaCl$) crystals from the adhered material. The overlap of the peaks of silicon dioxide and those of graphite made it difficult to distinguish one another, but a small peak at 44.5° diffraction angle clearly identified the presence of the graphite(See 〈Figure Appendix V-2-4〉 sample 4). The EDS results showed that the main component of the adhered material was oxides of aluminum, and the XRD results confirmed that the oxides of aluminum were amorphous.



〈Figure Appendix V-2-4〉 XRD results of the adhered material(stern)

CHNS elemental analysis(for analyzing the content of combustible elements in the adhered material) showed that nitrogen was absent, but carbon, hydrogen, and sulfur were present in amounts ranging from 0.64~3.00wt.%¹⁶⁾, 3.42~5.25wt.%, and 4.40~8.63wt.%, respectively(See 〈Table Appendix V-2-2〉). Combining this result with the EDS results, the adhered material was composed of solid-producing elements upon combustion such as aluminum, sodium, and silicon, and three gas-producing elements upon combustion, i.e. carbon, hydrogen, and sulfur. The hydrogen component appears to have come from the moisture.

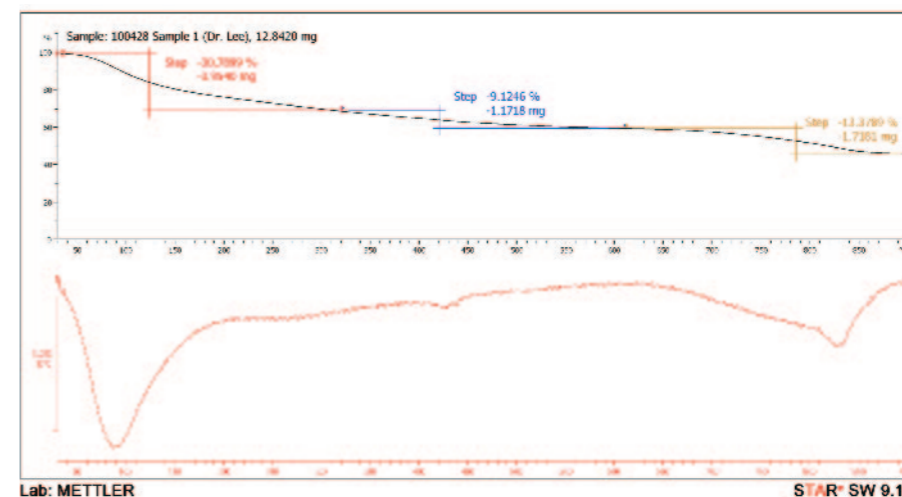
Sample name	Nitrogen(%)	Carbon(%)	Hydrogen(%)	Sulfur(%)
Sample 1	Below 0.01	0.64	4.45	5.21
Sample 2	Below 0.01	1.15	3.42	4.40
Sample 3	Below 0.01	3.00	4.56	4.87
Sample 4	Below 0.01	1.69	5.25	8.63

〈Table Appendix V-2-2〉 CHNS elemental analysis results

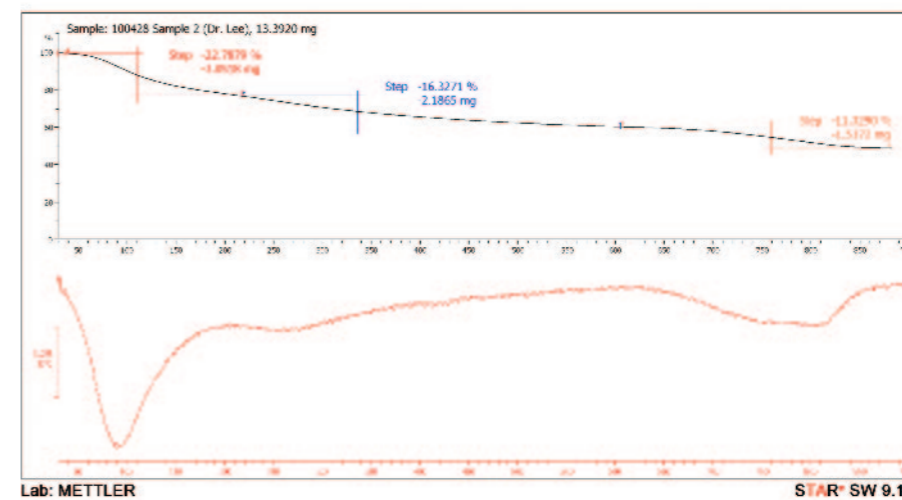
16) wt. % : weight %

The analysis of TGA pyrolysis for the adsorbed material was performed at temperature range of 30~900℃ and temperature increase rate of 10℃/min. The analysis on sample # 5 could not have been carried out due to shortage in the amount of the sample.

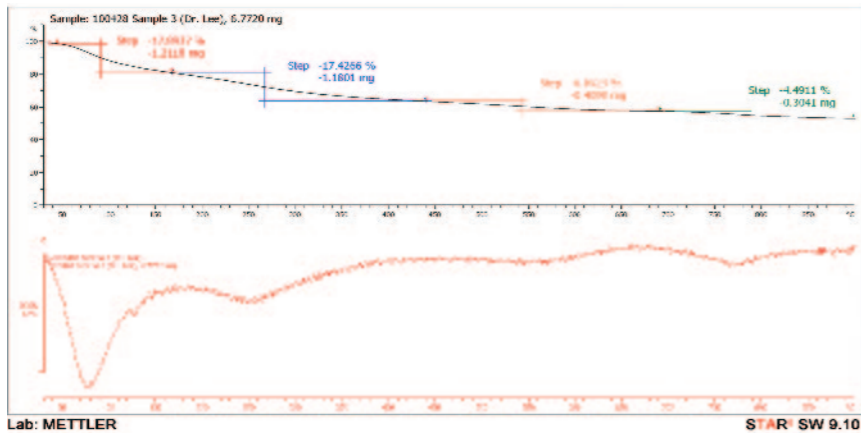
In a temperature range of 30 to 200℃, approximately 20% of the moisture evaporated. Additional 20% of the moisture evaporated slowly between 200℃ and 600℃. Above 600℃, carbon and sulfur components were oxidized and disappeared(See 〈Figure Appendix V-2-5〉). The detailed thermal analysis will be discussed later.



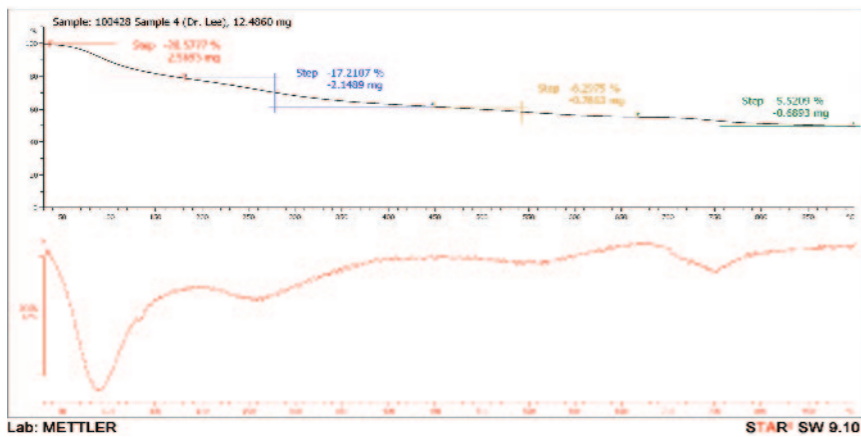
Sample 1



Sample 2



Sample 3



Sample 4

〈Figure Appendix V-2-5〉 TGA results of the adhered material(stern)

The analysis on the white adhered material of the stern showed that the adhered material was the agglomerates of fine particles, which was in good agreement with the assessment of the first analysis. It also showed that it consisted of mainly amorphous aluminum oxides with small amounts of sulfur or sulfur compounds along with salt and silicon dioxide. The composition was shown in 〈Table Appendix V-2-3〉. The water content was calculated using the hydrogen content obtained from CHNS-EA.

Component	Content(% weight)	Remarks
Al _x O _y	36.4 ~ 55.1	Contains small portion of silicon dioxide
Water	30.8 ~ 47.3	
Sulfur	4.4 ~ 8.6	
Carbon	0.6 ~ 3.0	Some portion of graphite
Salt	3.7 ~ 10.3	

〈Table Appendix V-2-3〉 Composition of the adhered material

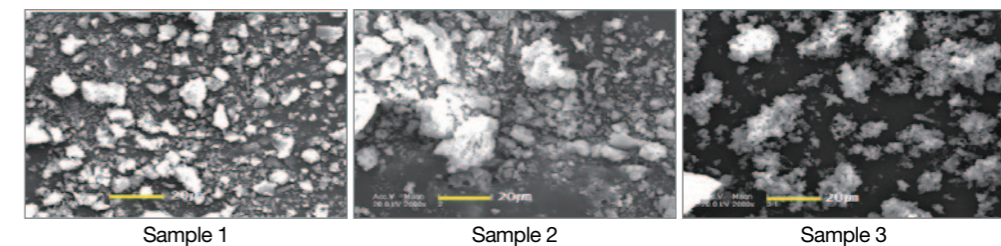
3. Third Analysis(Material Adhered on the Bow and Stack)

After visual identification of the bow on April 30, 2010, a similar adhered material was found; especially, an enormous amount of white powder was also observed on the inner and outer platings of the stack. To compare the composition of these white powders with the adhered material found on the stern, the JIG collected samples from two locations on the bow and one location on the stack as shown in 〈Table Appendix V-3-1〉.

Sample #	Collected Locations	Surface Material
1	76mm naval gun barrel	Iron
2	Portside entrance	Aluminum alloy
3	Stack	Aluminum alloy

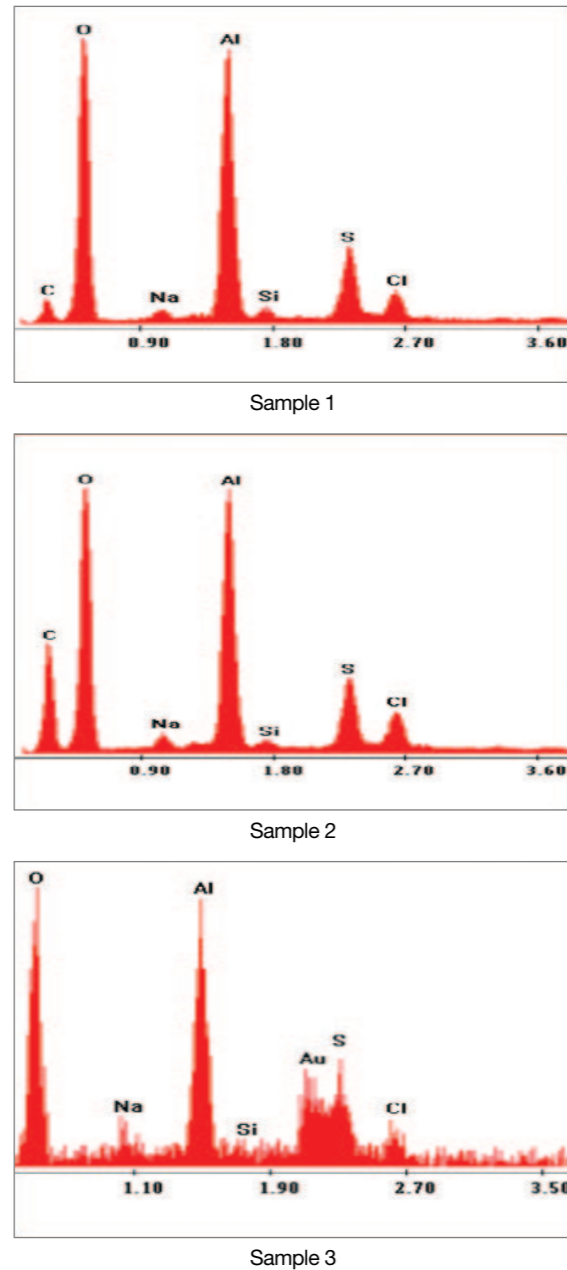
〈Table Appendix V-3-1〉 Sampling locations

The same equipments utilized in the first analysis were employed. The SEM images of this adhered material were similar to those of the stern(See 〈Figure Appendix V-3-1〉).



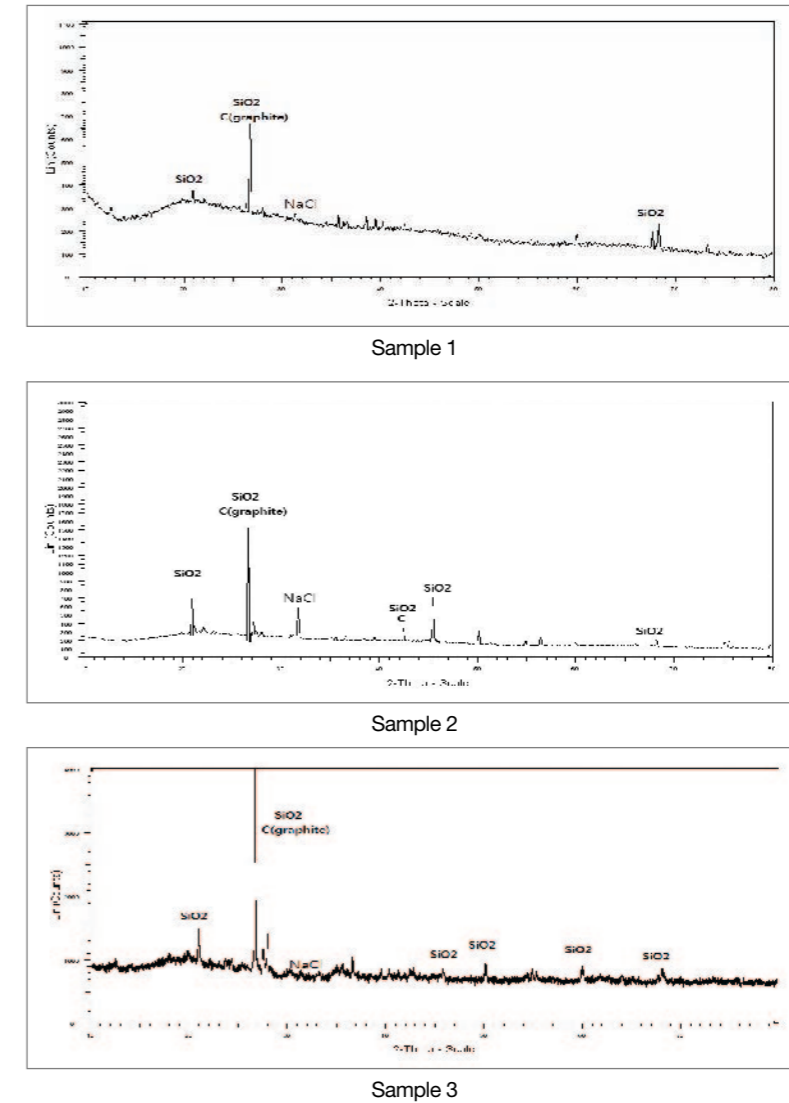
〈Figure Appendix V-3-1〉 SEM images of the adhered material(bow and stack)

As shown in <Figure Appendix V-3-2>, the EDS analysis results showed that the adhered material from both the bow and stack consisted of carbon, oxygen, sodium, magnesium, aluminum, silicon, sulfur, and chlorine. This result was similar to those of stern side samples.



<Figure Appendix V-3-2> EDS results of the adhered material(bow and stack)

The XRD results confirmed that silicon dioxide(SiO_2), graphite, and salt(NaCl) crystals were present from the adhered material and that the main component of the adhered material was oxides of aluminum. These results are in good agreement with those of stern sample(See <Figure Appendix V-3-3>).



<Figure Appendix V-3-3> XRD results of the adhered material(bow and stack)

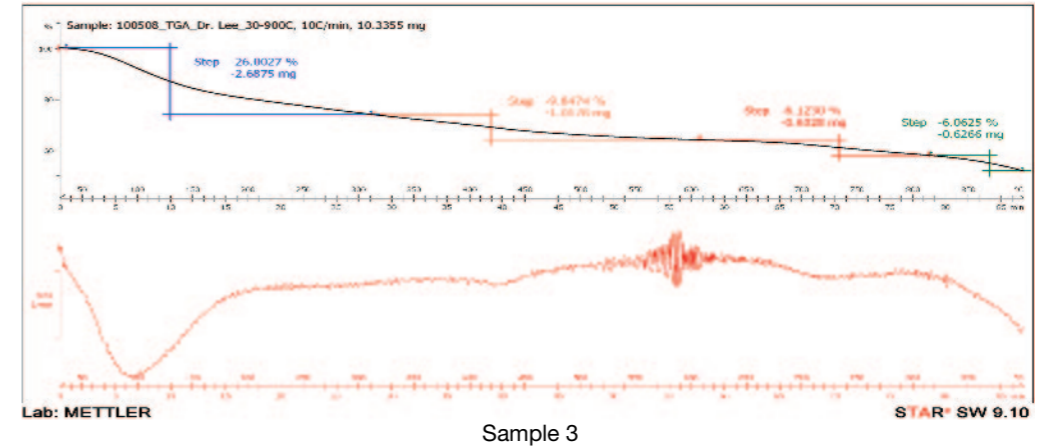
CHNS elemental analysis confirmed carbon, hydrogen, and sulfur to be 0.76~1.12wt.%, 3.62~3.93wt.%, and 2.43~3.58wt.%, respectively(See <Table Appendix V-3-2>), which was similar to those of the stern samples.

Sample name	Nitrogen(%)	Carbon(%)	Hydrogen(%)	Sulfur(%)
Sample 1	Below 0.01	0.76	3.93	3.50
Sample 2	Below 0.01	1.12	3.62	2.43
Sample 3	Below 0.01	0.84	3.63	3.58

〈Table Appendix V-3-2〉 CHNS elemental analysis results

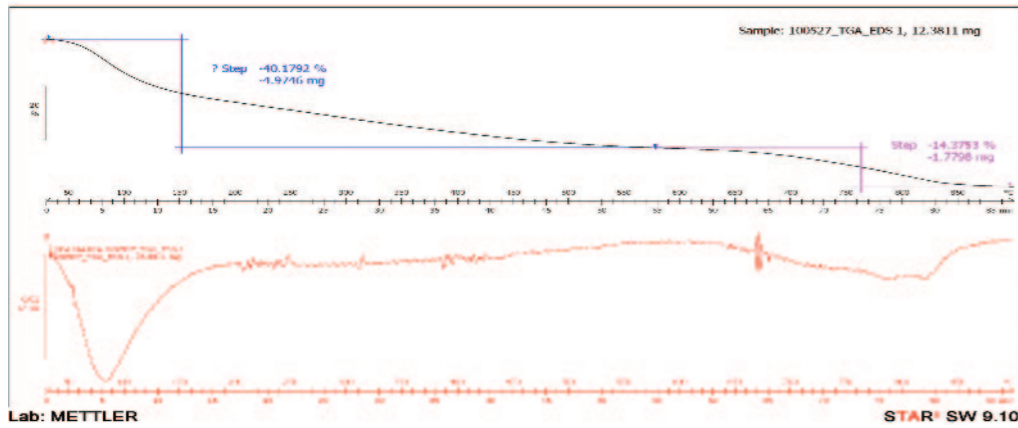
The same conditions for the TGA pyrolysis of the adhered material were employed as those of stern samples; namely, the temperature range of 30~900℃ and the temperature increase at the rate of 10℃/min.

The pyrolysis results were similar to those results from the stern samples(See 〈Figure Appendix V-3-4〉).

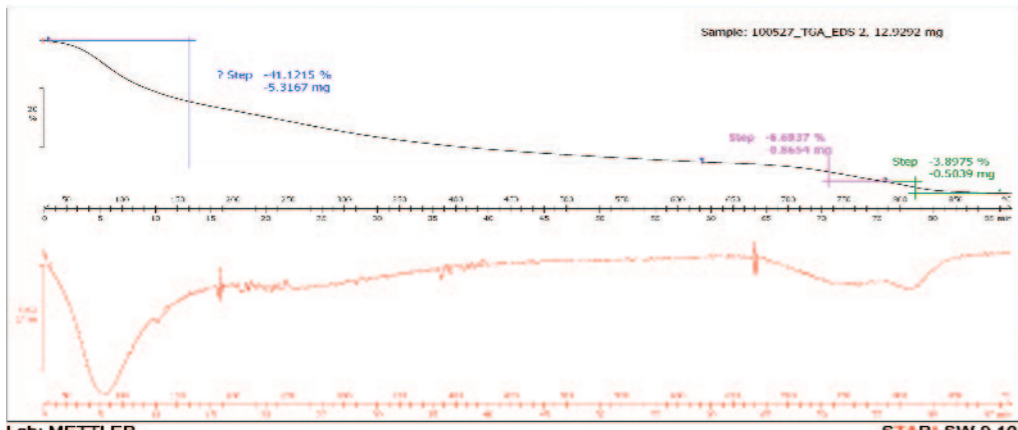


〈Figure Appendix V-3-4〉 TGA results of the adhered material(bow and stack)

The analysis results of the white adhered material on the bow and stack were identical to those of the stern samples, and the adhered material consisted of mainly amorphous oxides of aluminum and small amounts of sulfur or sulfur compounds along with salt and silica. The composition was shown in 〈Table Appendix V-3-3〉.



Sample 1



Sample 2

Component	Content(% weight)	Remarks
Al _x O _y	53.5 ~ 54.6	Contains small portion of silicon dioxide
Water	32.6 ~ 35.4	
Sulfur	2.4 ~ 3.6	
Carbon	0.8 ~ 1.1	Some portion of graphite
Salt	6.9 ~9.3	

〈Table Appendix V-3-3〉 Composition of the adhered material(bow and stack)

4. Fourth Analysis(Adhered Material on the Propulsion Section of the Torpedo)

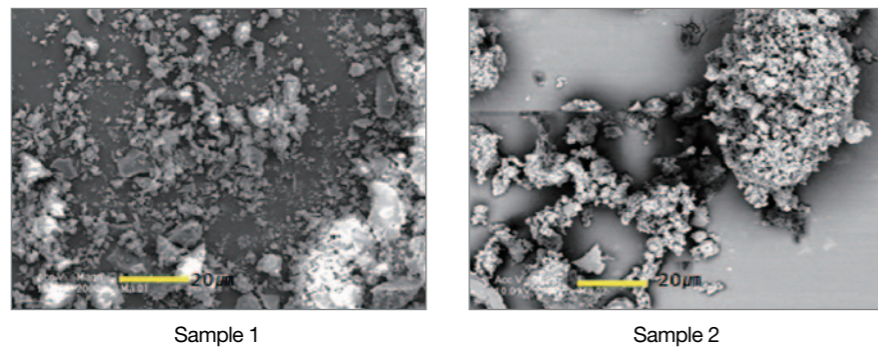
After visual examination of the propulsion motor system upon the salvage on May 15, white adhered material was found on the surface of propulsion section and inside the motor. Visually, it appeared to be the same material found in the fractured surfaces of ROKS Cheon-

nan. In order to investigate whether they were the same material as those found on ROKS Cheonan, the JIG collected samples from each part as shown in <Table Appendix V-4-1>.

Sample #	Location	Surface material
1	Salvaged torpedo propulsion section	Aluminum Alloy
2	Salvaged torpedo motor	Iron

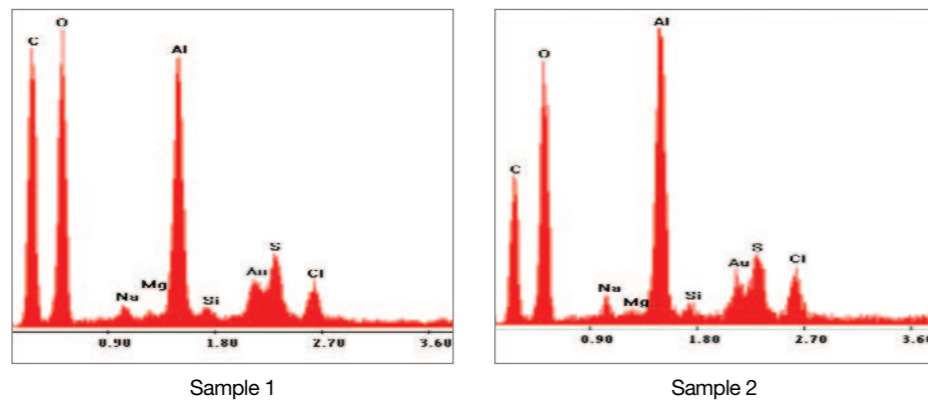
<Table Appendix V-4-1> Sampling locations

The analysis utilized the same apparatus used in the first and second analyses except elemental analysis, where the model EA1110 of CE Instruments was used. The SEM images of these two samples of the adhered materials were similar to those of hull samples.



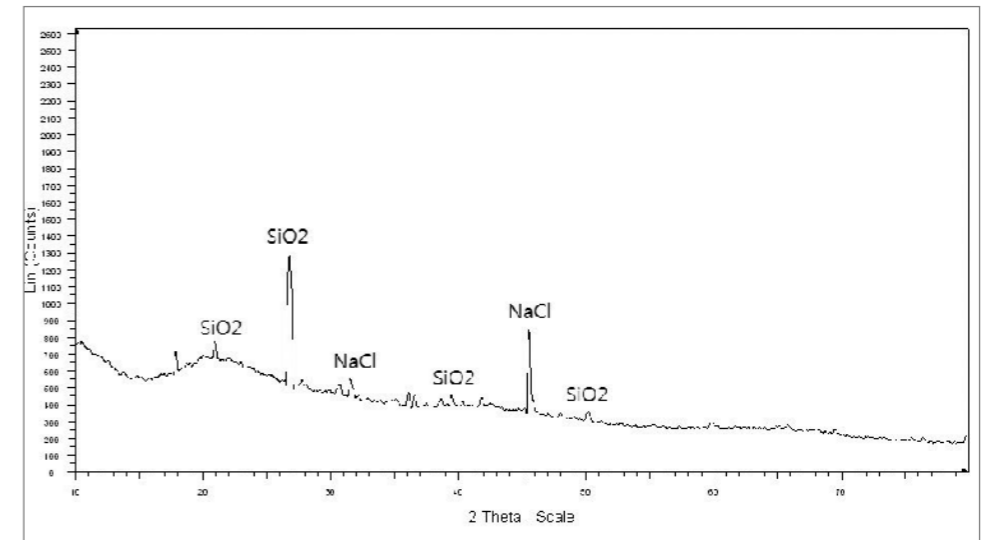
<Figure Appendix V-4-1> SEM images of the adhered material(propulsion section and motor)

As shown in <Figure Appendix V-4-2>, the EDS analysis results showed that the adhered material consisted of carbon, oxygen, sodium, magnesium, aluminum, silicon, sulfur, and chlorine. Those results were similar to those of hull samples.

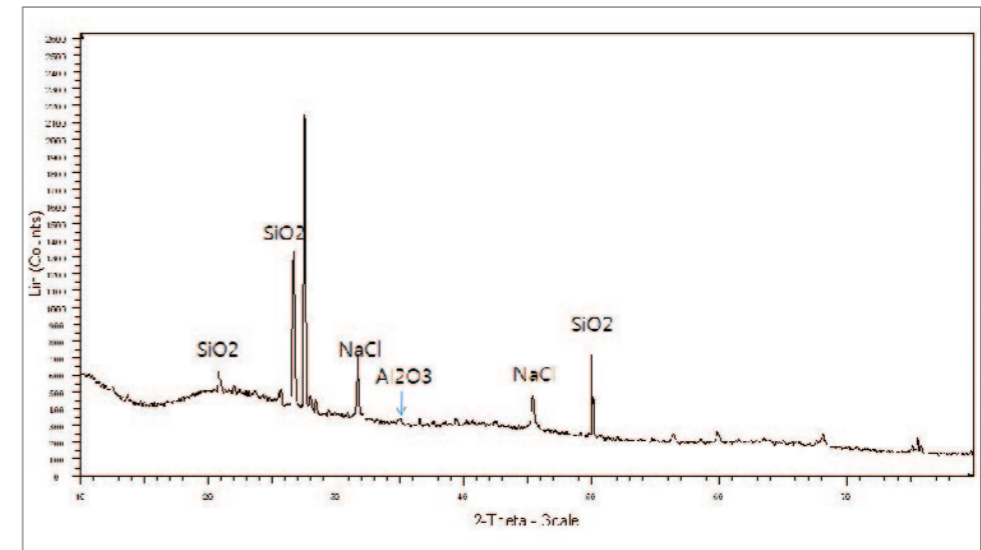


<Figure Appendix V-4-2> EDS results of the adhered material(propulsion section and motor)

The XRD results confirmed that silicon oxide(SiO_2) and salt(NaCl) crystals were present. The peak positions of the two samples were reasonably similar. Although the peak size was almost negligible, an aluminum oxide(Al_2O_3) crystal peak was also observed(See <Figure Appendix V-4-3>).



Sample 1

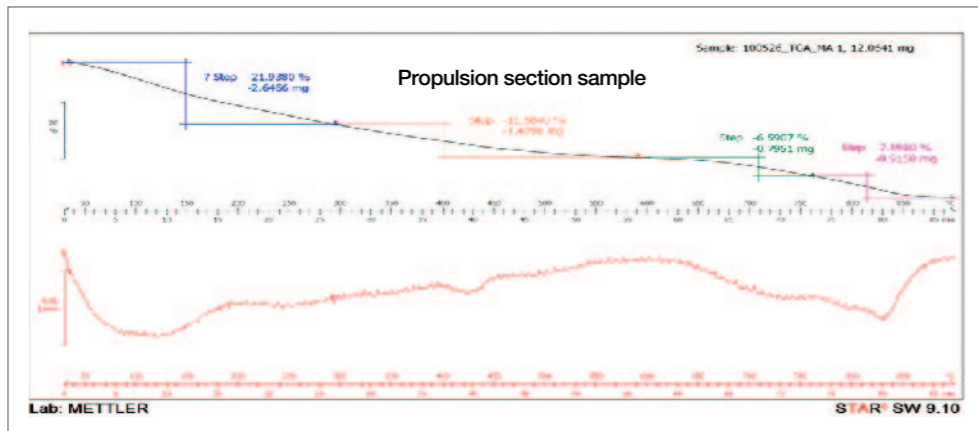


Sample 2

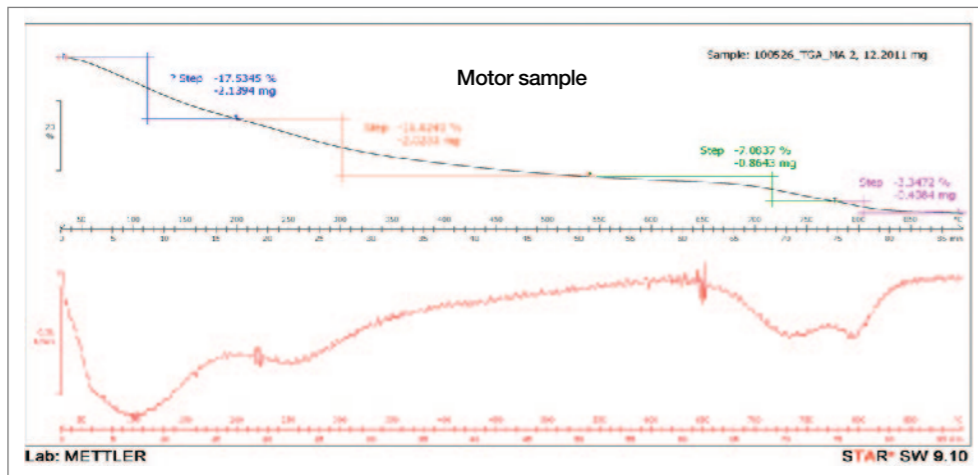
<Figure Appendix V-4-3> XRD results of the adhered material(propulsion section and motor)

Combining the EDS results with the XRD ones, the main component of the adhered material was oxides of aluminum, the majority of which was in amorphous form. These results concurred with those of stern samples.

The results of CHNS elemental analysis for identifying combustible elements showed that nitrogen was hardly found, and the contents of carbon, hydrogen, and sulfur were 0.40~0.86wt.%, 3.29~3.34wt.%, and 5.60~6.61wt.%, respectively. These results were similar to those of hull samples. In the TGA pyrolysis performed under the same analysis conditions with the hull samples, the results were similar to those of hull samples as well(See <Figure Appendix V-4-4>).



Sample 1



Sample 1

<Figure Appendix V-4-4> TGA results of the adhered material(propulsion section and motor)

As a summary of all the analysis results, the adhered materials from the propulsion section and the motor of the torpedo were the same type of material, and the adhered material consisted of mainly amorphous oxides of aluminum with a small amount of sulfur or sulfur compounds along with salt and silica. The composition is shown in <Table Appendix V-4-2>.

As will be discussed in the conclusion section, it was assessed that the adhered material was a product of underwater explosive with a substantial portion of aluminum.

Component	Content(% weight)	Remarks
Al _x O _y	53.9 ~ 54.3	Contains small portion of silicon dioxide
Water	29.6 ~ 30.1	
Sulfur	5.6 ~ 6.6	
Carbon	0.4 ~ 0.9	
Salt	8.6 ~ 10.1	

<Table Appendix V-4-2> Composition of the adhered material(propulsion section and motor)

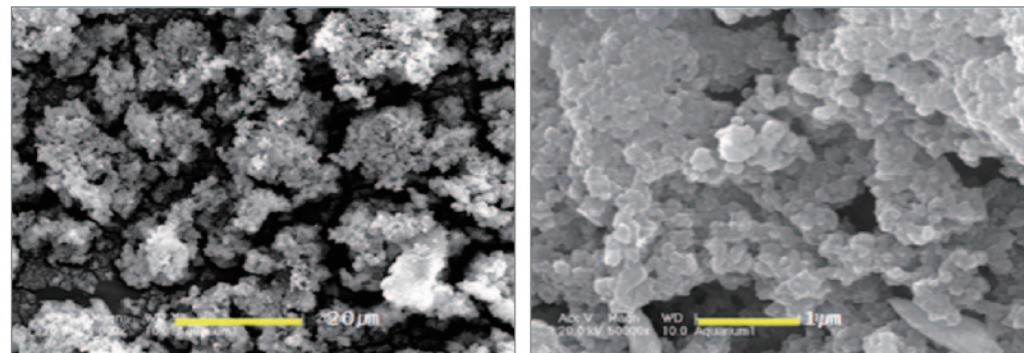
5. Fifth Analysis(Material Acquired from Small-scale UNDEX Experiment)

The analysis conducted small-scale UNDEX experiments in order to compare the adsorbed material found on the hull and torpedo with the explosion products from an underwater explosive formulation containing aluminum.

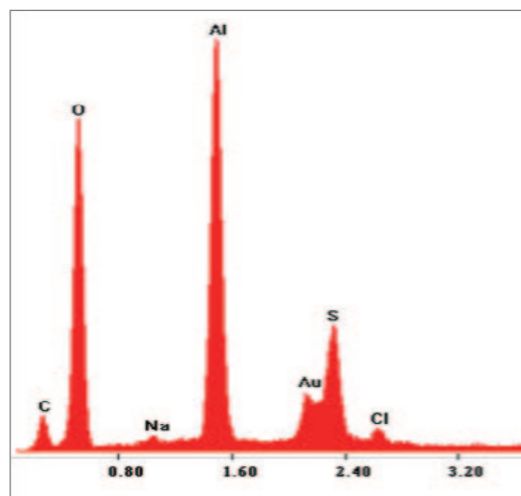
A water tank of 2m length × 1.5m width × 1.5m height was used with transparent polycarbonate window on the front side, and it was filled with 4.5 tons of sea water. An aluminum plate was installed on top of the tank in order to collect the samples, and detonated 15 grams of HBX-3 explosive(TNT 29%, RDX 36%, Al 35%) in the center of the tank. The propagation of the shockwave and the expansion-contraction-elevation processes of the bubble were observed through a high-speed camera. After the explosion, a small amount of explosion products(a few milligrams) was adsorbed on the plate. Since adsorbed samples were too small, the XRD analysis, which requires a relatively larger amount of samples, was conducted using the aluminium plate itself with explosion products adsorbed on

its surface. For the EDS analysis, the adsorbed material was extracted from the plate.

The adsorbed samples were agglomerates of fine particles. The sizes of the fine particles were less than a micrometer (See <Figure Appendix V-5-1>). According to the EDS results shown in <Figure Appendix V-5-2>, the samples obtained from small-scale UNDEX experiment consisted of carbon, oxygen, sodium, magnesium, aluminum, silicon, sulfur, and chlorine. The results were almost identical to the compositions from the hull and torpedo samples.

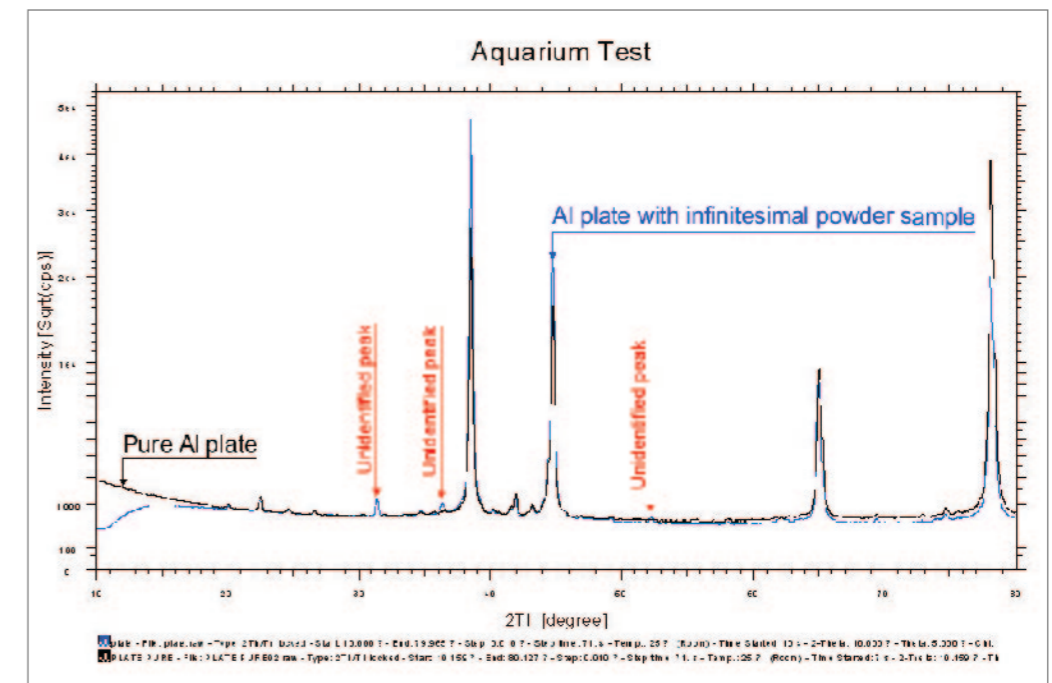


<Figure Appendix V-5-1> SEM images of the explosion products

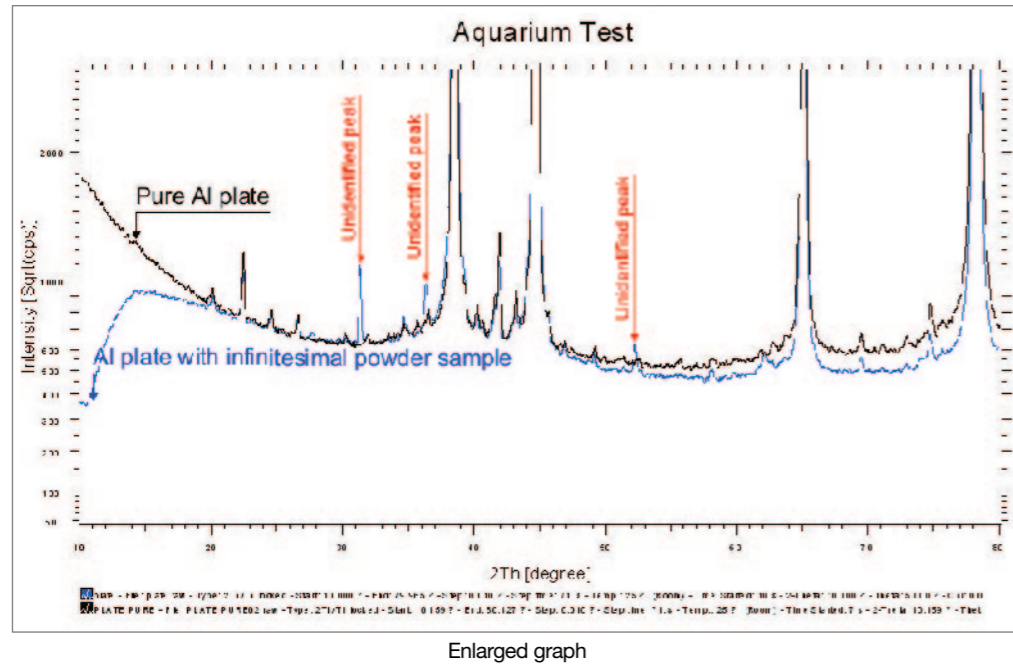


<Figure Appendix V-5-2> EDS analysis of UNDEX sample

Since XRD analysis was conducted using the aluminum plate with a small amount of underwater explosion products adsorbed on the surface, the aluminum crystal peak became apparent while the peaks of other substances were relatively weak in comparison. In <Figure Appendix V-5-3>, the XRD result of the explosion products adhered to an aluminum plate was depicted along with the one of the aluminum plate only. When the weak peaks were magnified, crystalline aluminum oxide was rarely observed. This happened because nearly all of the oxides of aluminum were found in amorphous form, which did not appear in the XRD analysis. Other weak peaks were identified to be irrelevant to the aluminum oxide. Through these analysis results, it was found that underwater explosive formulations containing aluminum powder produced amorphous oxides of aluminum upon explosion, as were also found in the hull and torpedo samples. However, the compositions of the explosion products may vary depending on the composition of underwater explosive formulations, amount of explosives, and condition of explosion.



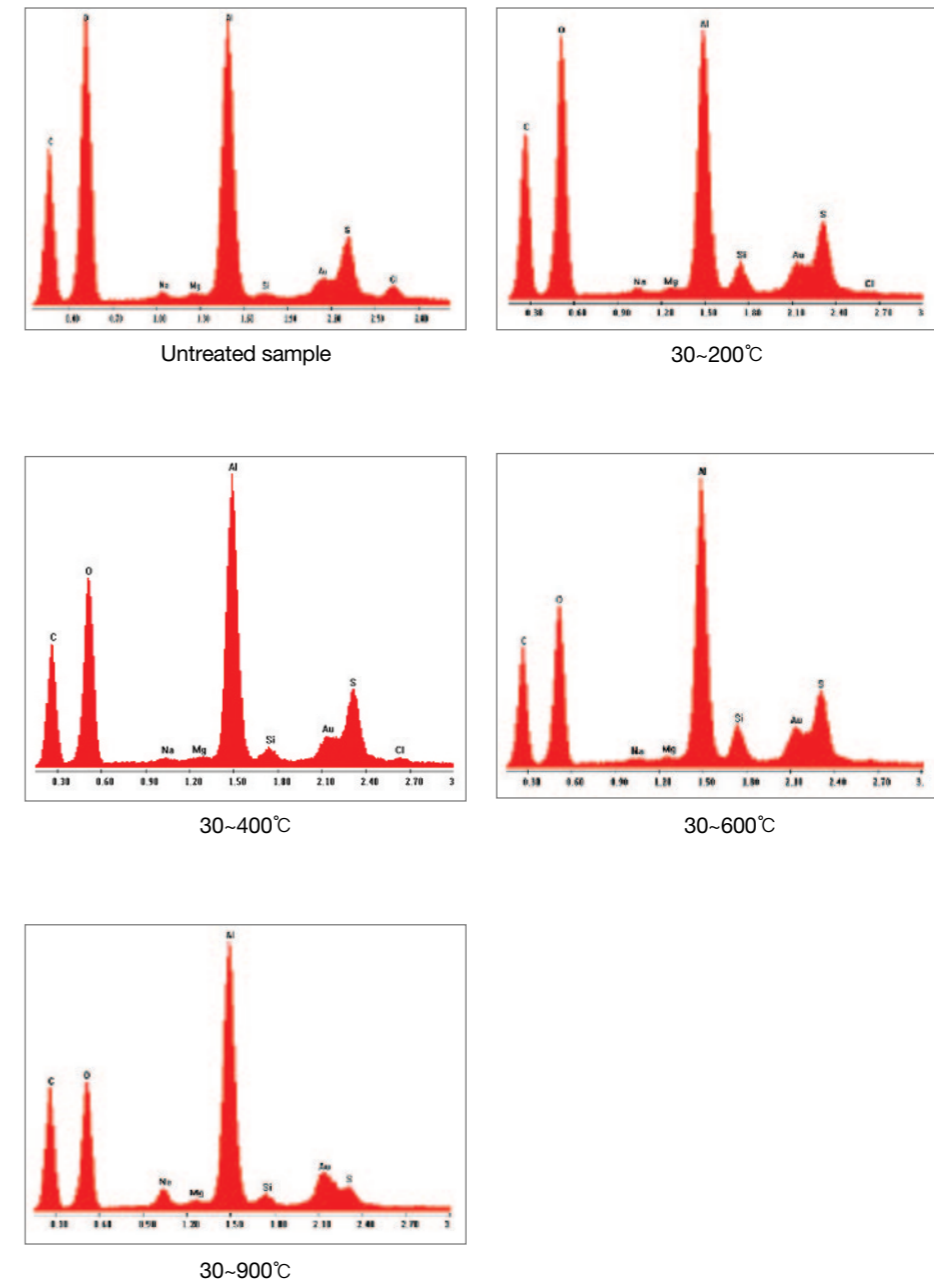
Original graph



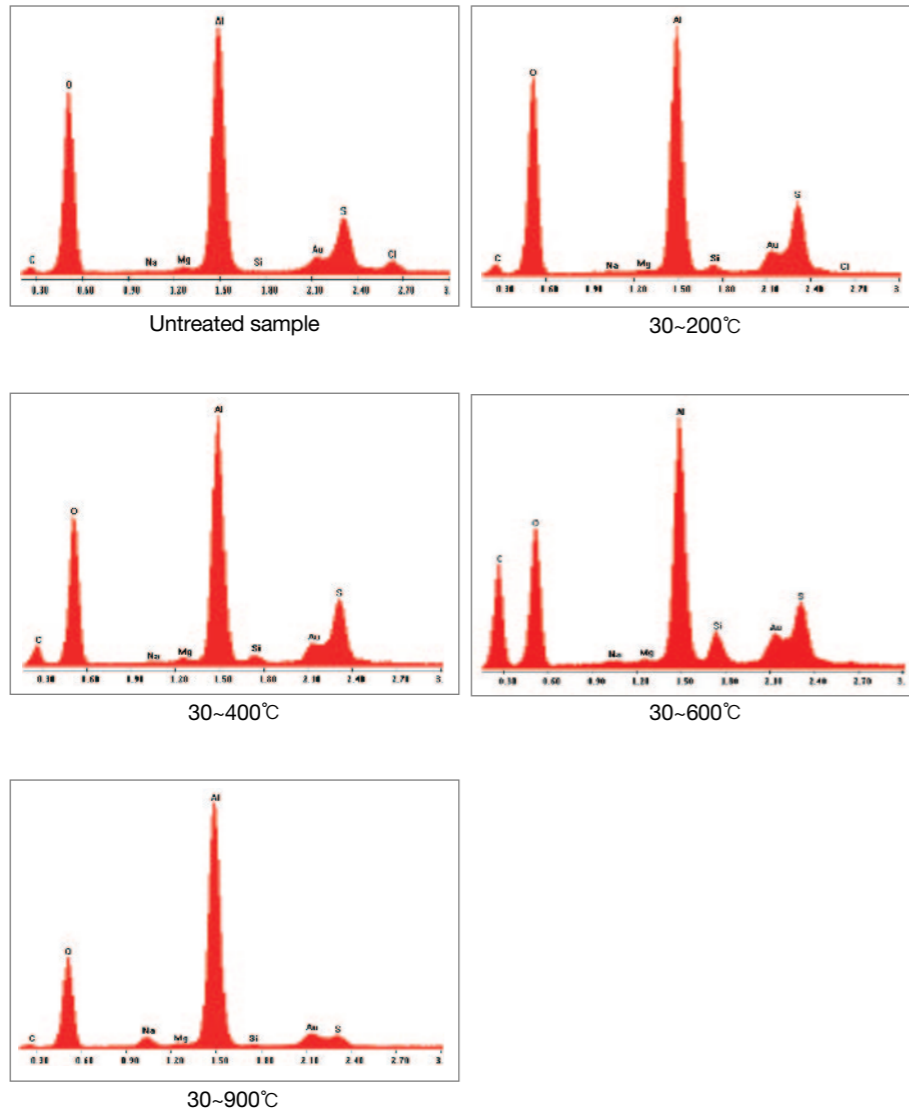
〈Figure Appendix V-5-3〉 XRD results of the explosion products

6. Thermal Characteristics and Microstructure of the Adhered Material

The analysis pyrolyzed the adhered material at different temperature ranges (30~200 °C, 30~400 °C, 30~600 °C, 30~900 °C) under nitrogen atmosphere and subsequently performed the EDS analysis with pyrolyzed products in order to comprehend thermal characteristics of the adhered material. The analysis areas for the EDS analysis were 0.25mm × 0.20mm, or 0.50mm × 0.40mm (See 〈Figure Appendix V-6-1〉). In addition, the team also performed a spot analysis with the agglomerate of particles (See 〈Figure Appendix V-6-2〉) and compared with the area analyses. When two different sets of EDS results were compared, the difference of carbon compositions was attributed to the adhesive tape used in the area analysis. Accordingly, the oxygen composition was also changed slightly.



〈Figure Appendix V-6-1〉 Change of elemental composition of adhered materials in EDS area analysis with different heat treatment



〈Figure Appendix V-6-2〉 Change of elemental composition of adhered materials in EDS spot analysis with different heat treatment

As was shown in two figures, mainly the oxygen content was decreased between 30 and 600°C. Upon further increase of the temperature, carbon and sulfur disappeared.

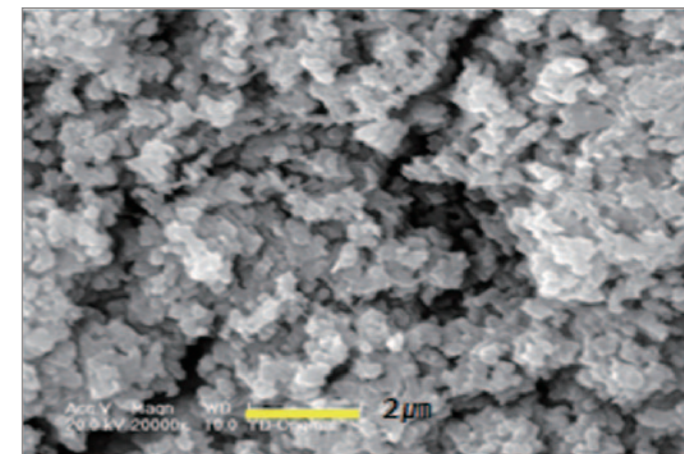
In 〈Table Appendix V-6-1〉, compositions of oxygen and aluminum are summarized in both area and spot analyses in different temperature ranges. Elemental composition was calculated by considering the oxygen content in silica. Oxygen/aluminum ratio of the sample pyrolyzed from 30 to 200°C was quite similar with that of the unpyrolyzed sample.

This happened due to the evaporation of the moisture in the treatment of samples including vacuum at the EDS analysis of the unpyrolyzed sample. TGA analysis showed that approximately 50% of the moisture evaporated in the temperature range of 30 to 200°C. Further increase of the pyrolysis temperature prompted the oxygen content to diminish due to the evaporation of the moisture entrapped in micro pores (See 〈Figure Appendix V-6-3〉) and/or strongly interacted with the adhered material.

Generally, it is known that EDS analysis on a mixture of ununiform particles cannot give an accurate quantitative information on the element composition. In this regard, 〈Table Appendix V-6-1〉 shows the qualitative trend of change in oxygen and aluminum composition with heat-treatment temperature.

Sample Name	Area Analysis		Spot Analysis	
	O(Atom %)	Al(Atom %)	O(Atom %)	Al(Atom %)
Raw sample	72.90	27.10	68.24	31.76
30~200°C	71.29	28.71	69.31	30.69
30~400°C	65.93	34.07	64.42	35.58
30~600°C	61.05	39.95	61.39	39.61
30~900°C	60.57	39.43	56.80	43.20

〈Table Appendix V-6-1〉 Change of O/Al composition ratio in EDS analysis with different heat treatment

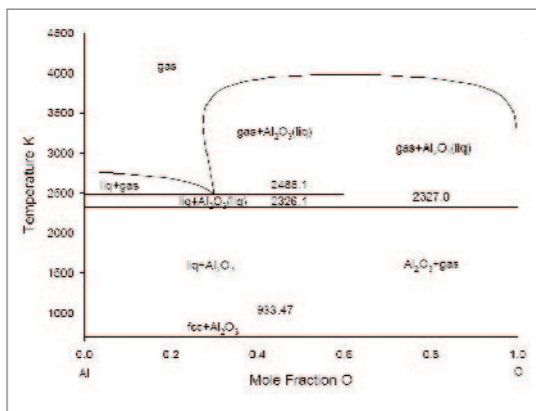


〈Figure Appendix V-6-3〉 Microstructure of the adhered material

7. Amorphous aluminum oxide

As mentioned previously, pure aluminum becomes covered with a very thin (several nm) film of amorphous aluminum oxide in a short time upon production. This amorphous aluminum oxide film is too dense for oxygen to penetrate, and prevents further oxidation inside the film. However, when it is exposed to the moisture, alkalies, or acids for a long time, it undergoes further oxidation to form a white product, the main compositions of which are aluminum hydroxide ($\text{Al}(\text{OH})_3$, bayerite), boehmite ($\text{AlO}(\text{OH})$), and aluminum oxide (Al_2O_3). This corrosion product is not in amorphous form, but rather in a crystalline form. There have been numerous reports that corrosion products become crystalline oxides of aluminum when aluminum is corroded by sea water or salinity in the shore.

To produce amorphous aluminum oxide (Al_xO_y), aluminum oxide should be liquid when produced, and be cooled rapidly. It is impossible to make amorphous by cooling the solid. <Figure Appendix V-7-1> illustrates the phase diagram of aluminum oxide according to the change of composition ratio between aluminum oxide and oxygen, and shows that Al_2O_3 exists as liquid above 2325.1°C and stays as solid below 2325.1°C . Thus, to be amorphous, aluminum oxide should be liquified at the temperature of higher than 2325.1°C and cooled rapidly.



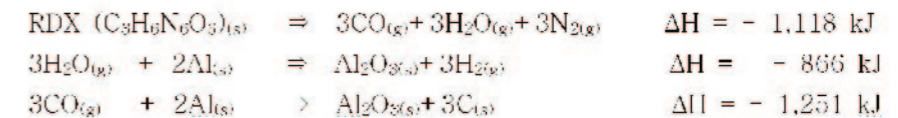
<Figure Appendix V-7-1> AL-O Binary Phase Diagram¹⁷⁾

17) Yajun Liu, "The Kinetics of Incongruent Reduction Between Sapphire and Mg-Al Melts" Phd Thesis, Georgia Institute of Technology, 2006.

Besides the condition mentioned above, aluminum oxide becomes amorphous if it is not able to form proper crystalline lattices by reacting between aluminum and oxygen with improper stoichiometry.

Thus, amorphous aluminum oxide (Al_xO_y) is produced by either explosions or plasma reactions, which accompany rapid oxidation, high temperature heating, and rapid cooling.

Aluminum oxide is usually incorporated to underwater explosive formulations to augment bubble energy by using high combustion energy of aluminum. Explosion reactions take place in less than 10 microseconds at the temperature of higher than $3,000^\circ\text{C}$ and the pressure above 200,000 atm. During an explosion, aluminum powder reacts with the oxygen in the explosion products, and is subsequently converted to aluminum oxides generating a large quantity of heat. The chemical reaction scheme to form aluminum oxide from explosion is shown as below. This aluminum oxide produced is cooled at a rate of several tens to hundreds thousand degrees per second less than several tens milliseconds.

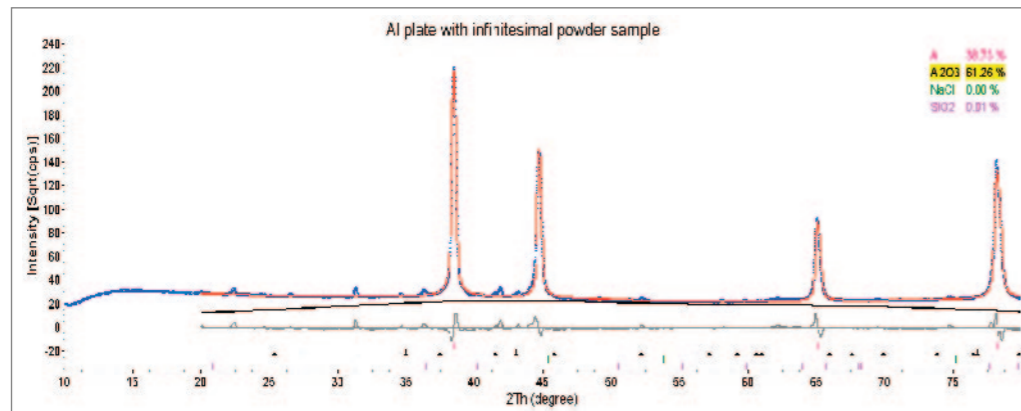
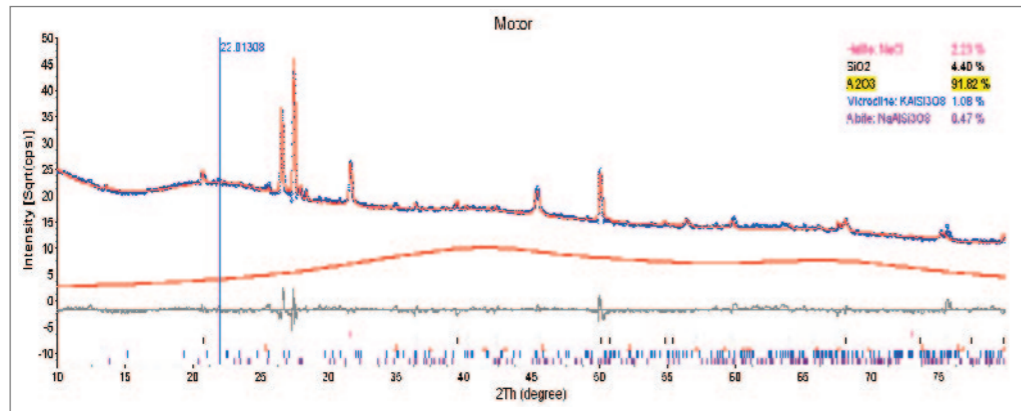
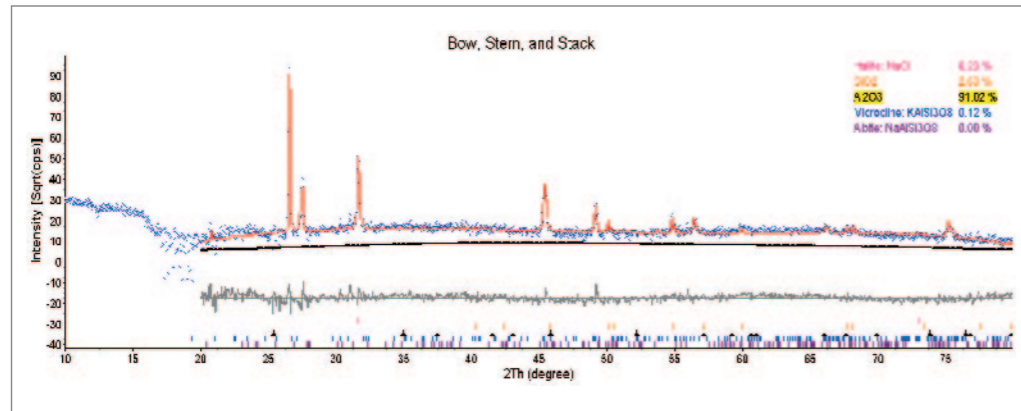


Aluminum oxide which is produced as a component of explosion products from aluminum based explosive formulations is known to be amorphous. As explained previously, producing amorphous aluminum oxide by explosion is attributed to the reaction between aluminum and oxygen with improper stoichiometry in an extremely fast oxidation (explosion), and/or the formation of improper crystalline lattices in a rapid cooling process from liquid to solid.

In order to identify whether aluminum oxide of the adhered material was amorphous, a detailed XRD analysis was performed with the TOPAS program¹⁸⁾ and pyrolysis experiments of the adhered material.

According to the detailed XRD analysis with the TOPAS program, the adhered materials from both the hull of ROKS Cheonan and torpedo propulsion section were composed of more than 90% of amorphous aluminum oxide. In addition, explosion products of UNDEX experiments were also analyzed to have mostly amorphous aluminum oxide, except crystalline ones from the aluminum plate (See <Figure Appendix V-7-2>).

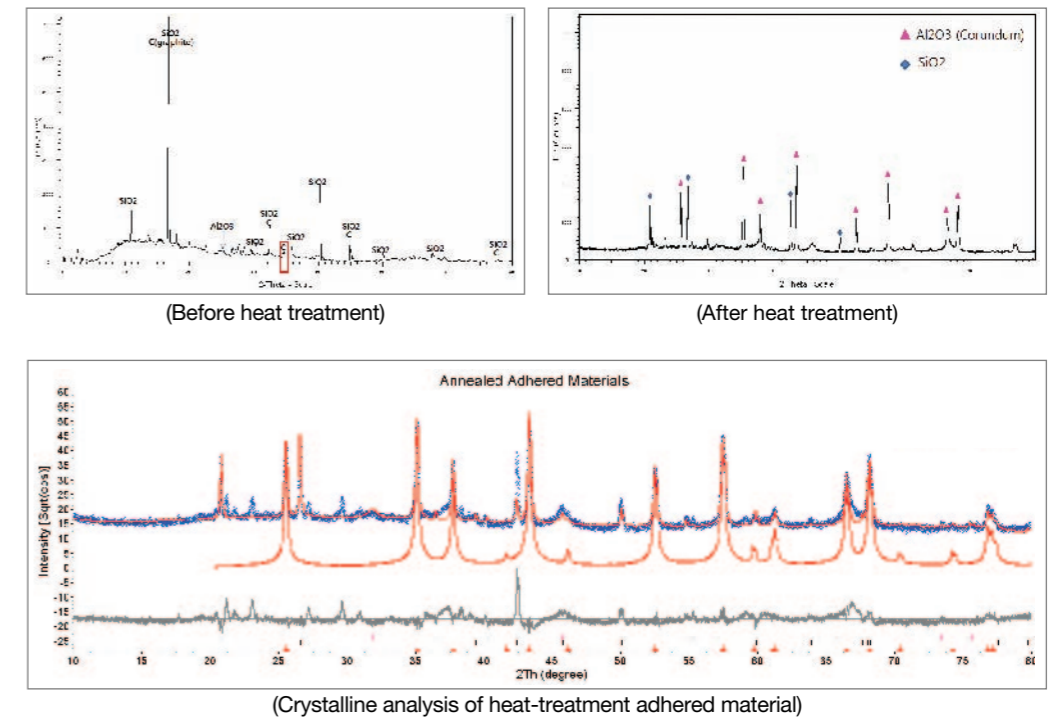
18) TOPAS program: Stands for Total Pattern Analysis Solution, and is a software used to analyze the X-ray diffraction data.



〈Figure Appendix V-7-2〉 Analysis of amorphous Al_2O_3 content

In general, amorphous materials are usually transformed to crystalline ones by heat treatment at an appropriate temperature below the melting point. If a crystalline aluminum oxide is found in heat-treated material, in which no crystalline aluminum oxide nor crystalline aluminum was found originally, the material should have an amorphous aluminum oxide as an ingredient in it. To comprehend this, the adhered material collected from the hull of ROKS Cheonan was heated to 1,200 °C for 30 min. and cooled slowly in an ambient condition. The change of crystallinity before and after the heat treatment was compared.

The XRD results depicted in 〈Figure Appendix V-7-3〉 showed that the main component of the adhered material before the heat treatment was silica (including a small amount of graphite), and crystalline aluminum oxide (Al_2O_3) was produced and graphite disappeared after the heat treatment. Thus, the adhered material should be produced by either rapid oxidation or rapid cooling.



〈Figure Appendix V-7-3〉 XRD results of the adhered material before and after heat treatment

8. Analysis Result

White powders adhered on the hull and the parts of the torpedo were confirmed to be explosion products formed by the detonation of an underwater explosive formulation with aluminum. They were not corrosion products of aluminum.

The following provides findings that can rule out the possibility of the adsorbed materials as corrosion products of aluminum from ROKS Cheonan or the torpedo motor. The adhered materials were:

- Adhered in large amounts to non-aluminum surface as well.
- Adhered not firmly, and could be detached easily.
- Were not combined closely, and easily disintegrated.
- Mainly composed of amorphous aluminum oxides.
- In amorphous form, and white corrosion product of aluminum is normally crystalline.

In addition, reasons supporting the adhered material as explosion formulation are listed as follows:

- The major component of adhered material was amorphous aluminum oxide, and appeared not to be originating from ROKS Cheonan herself.
- No scientific reasons for the formation of amorphous aluminum oxide underwater were found.
- Graphite was detected as well.
- Amorphous aluminum oxide is produced when aluminized explosives explode.¹⁹⁾
- Amorphous carbon, graphite, and diamond are produced upon explosion of most explosives.

.....
19) R. R. McGuire. et. al., 'Detonation Chemistry: An Investigation of Fluorine as An Oxidizing Moiety in Explosives', Lawrence Livermore Laboratory, AD A119092, N00014-77-F-0053, July 7, 1982.

Appendix VI. Stability Analysis Result

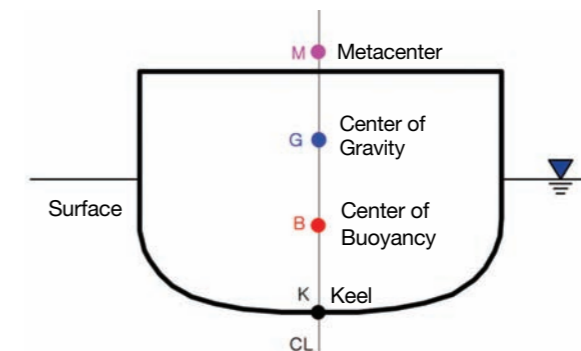
1. Objective

Analysis on stability was conducted in order to assess the warship design qualification of ROKS Cheonan equivalent class of corvette in perspective of a stability standard, and to technically clarify the details in sinking of the stern and bow after the separation.

Standard assessment of the stability design was conducted under several conditions: a normal operation before damage, and damage conditions with 2~4 adjacent compartments being flooded. The damage addressed here only implies flooding on the damaged regions while maintaining the longitudinal strength of the hull without separation. This assumption to assess the stability also applies to an ordinary merchant vessel as well as the warships.

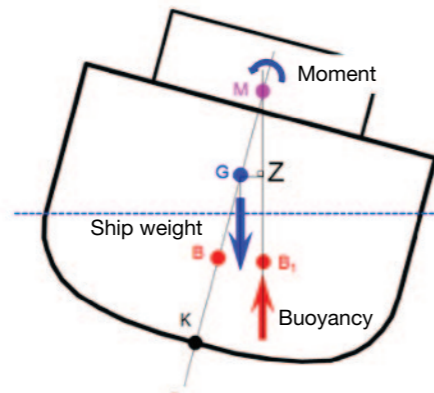
However, ROKS Cheonan was split and separated centering around the gas turbine room, and the stern sank rapidly while the bow sank after being capsized 90 degrees to the starboard side. In order to technically examine the conditions that can cause the sinking, the stability analysis on each of the bow and stern after the separation was also conducted.

2. Overview on Ship Stability



〈Figure Appendix VI-2-1〉 Stability factors

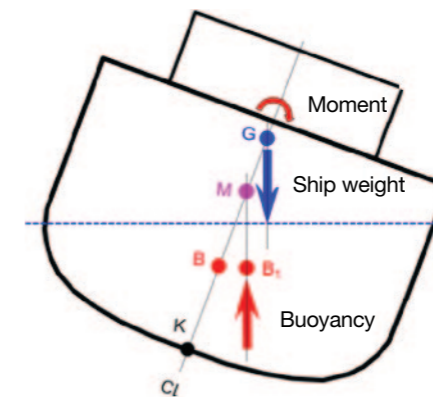
Major factors that influence the stability analysis include the center of gravity(G), center of buoyancy(B), and metacenter(M) as displayed in <Figure Appendix VI-2-1>. When both points G and B lie on a vertical line, the ship is balanced, hence in equilibrium. Ships are usually symmetrical in weight and geometrical shape, and thus points G and B lie on a vertical line that passes through the keel.



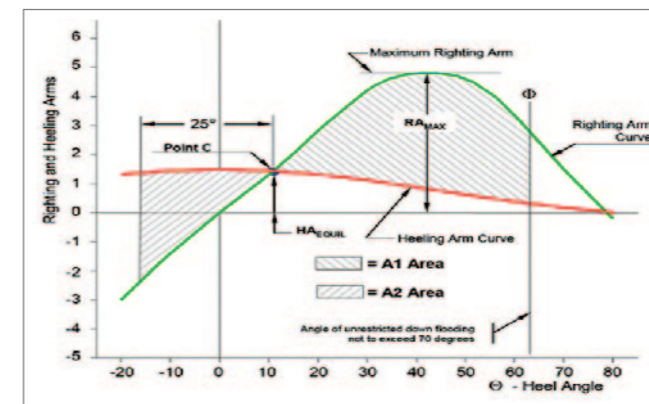
<Figure Appendix VI-2-2> Positive(+) stability

As shown in <Figure Appendix VI-2-2>, when a ship inclines to a transverse angle, the center of buoyancy moves to B1, the vertical line before the tilt(line through K-B-G) and the vertical line through B1 after the inclination cross each other at the point defined as the metacenter(point M on the Figures Appendix VI-2-1 and VI-2-2). If point M is located above point G as shown in <Figure Appendix VI-2-2>, the moments produced by gravity and buoyancy in an inclined state would move in the opposite direction from the inclining direction, and thus the ship would be stabilized. This is defined as having a positive stability($GM > 0$). On the other hand, as displayed in <Figure Appendix VI-2-3> if M is located below G in a tilted state, the moment generated by gravity and buoyancy will move in the inclining direction, causing the ship to capsize. In this condition, the ship is “unstable” and this state is defined as a negative stability($GM < 0$). Therefore, the position and distance of points G and M along a vertical line become a critical factor in determining static stability of a ship. The magnitude of the moment to stabilize a ship is described as the length of the line, GZ, shown in <Figure Appendix VI-2-2>. This is defined as the righting arm, and it is possible to draw a curved shape depending on the inclination angle of a ship. Meanwhile, a ship could be heeled due to the effects of wind and wave. After estimating

the heeling moment(The heeling arm is defined as the heeling moment divided by the displacement of the ship) by the wind pressure and wave along with the list angle, and overlapping with the righting curve addressed earlier, the curve shown in <Figure Appendix VI-2-4> can be obtained. The area A1 represents the stabilizing energy and A2 represents the capsizing energy; when $A1/A2$ is larger than 1, the ship is assessed to have a dynamic stability.



<Figure Appendix VI-2-3> Negative(-) stability

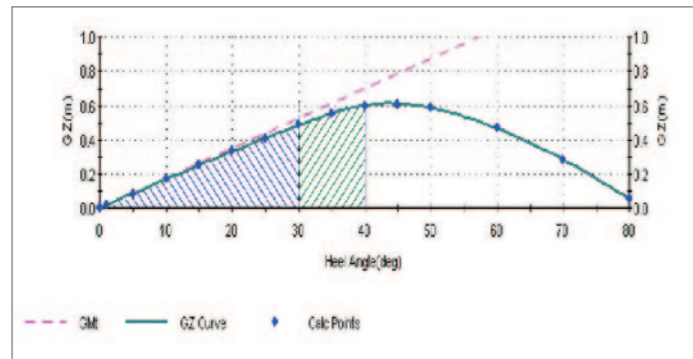


<Figure Appendix VI-2-4> The righting arm curve overlapped with the heeling arm curve, displaying a dynamic stability of a vessel

3. Stability Before the Damage

1) Static Stability

The stability arm curve representing the static stability of ROKS Cheonan is computed as shown in <Figure Appendix VI-3-1>.



<Figure Appendix VI-3-1> The righting arm curve of ROKS Cheonan prior to the damage

Category	US Navy	UK Navy	Merchant vessel	ROKS Cheonan
Area of shaded region under righting arm curve	0° ~ 30°	None	≥ 0.080 m · rad	0.18
	0° ~ 40°	None	≥ 0.133 m · rad	0.30
	30° ~ 40°	None	≥ 0.048 m · rad	0.12
Max righting arm curve angle	None	Above 30°	Above 25°	45°
GM(horizontal metacenter height)	None	0.3m	0.15m	Appx. 1.0m

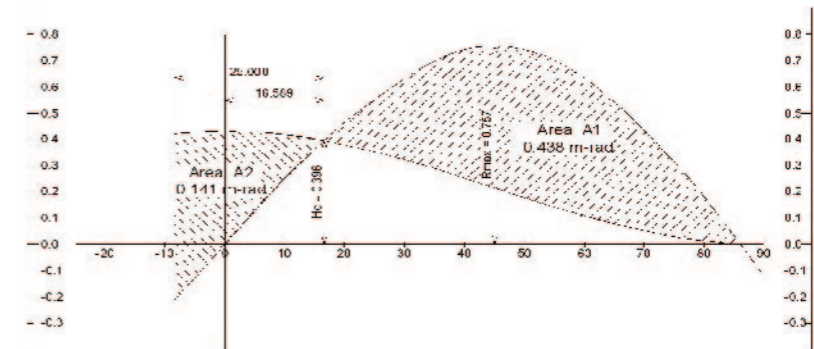
<Table Appendix VI-3-1> Static stability analysis result of ROKS Cheonan before the damage

A comparison between the static stability of ROKS Cheonan with the standards of UK Navy and merchant vessel is summarized in <Table Appendix VI-3-1>(Note: static stability standard is not established in the US Navy Standard). Through this result, it can be assessed that the static stability level of ROKS Cheonan before the damage was well above than that of a merchant vessel and twice as stable compared to the UK Navy stan-

dard. Prior to the damage, the hull stability was maximized at the heeling angle of 45°, and could endure the heeling angle of up to 80°.

2) Dynamic Stability

The righting arm curve overlapped with the heeling arm curve displaying the dynamic stability of ROKS Cheonan is depicted in <Figure Appendix VI-3-2>.



<Figure Appendix VI-3-2> The righting arm curve and the heeling arm curve

Category	US Navy design standard	UK Navy design standard	Merchant vessel design standard	Result on ROKS Cheonan
Wind speed(Knots)	90 knots	90 knots	50 knots	90 knots
Capsizing force vs. stability ratio(A1/A2)	Above 1.4	Above 1.4	Above 1.0	3.1

<Table Appendix VI-3-2> Dynamic stability analysis result prior to the damage

<Table Appendix VI-3-2> summarizes the dynamic stability of ROKS Cheonan before the damage in comparison with US, UK Navy and merchant vessels. The result indicates that the stability level of ROKS Cheonan prior to the damage was well above the standards for a merchant vessel and was competitive enough in comparison to the US and UK Navy standards.

4. Stability Analysis of ROKS Cheonan after the Damage

1) Damage Stability Standard

〈Table Appendix VI-4-1〉 displays the damage stability standard applied to ROKS Cheonan in comparison with merchant vessels. ROKS Cheonan is designed to survive against up to 30 knots of beam wind with two compartments being flooded. In the analysis, the result with two flooded compartments amply suffices the stability standard, but in order to measure the maximum stability, a further analysis of stability with three and four inundated compartments was conducted.

Category	Type	Dynamic stability standard	Damaged compartments(standard)
Passenger	-	Wind speed 25 knots	2 Compartments
Chemical liquid transportation	-	-	2 Compartments
Gas transportation	LNG	-	2 Compartments
	LPG	-	1 Compartment
Oil tanker	Length 150m & above	-	2 Compartments
	Length shorter than 150m	-	1 Compartment
Corvette class standard	-	Wind speed 30 knots	2 Compartments

〈Table Appendix VI-4-1〉 Damage stability standards in different types of ships

A number of damage conditions were considered to assess the damage stability of ROKS Cheonan under flooding. For the cases with damages in two compartments, the most hazardous conditions were considered in terms of stability: Case 1 assumes flooding of the gas turbine and diesel engine rooms, and Case 2 supposes simultaneous flooding of the diesel engine room with 1 adjacent aft compartment. For the cases of three compartments flooded, Case 3 presumes simultaneous flooding of the diesel engine room and 2 adjacent aft compartments, and Case 4 assumes inundation in the gas turbine, diesel engine and 1 adjacent aft compartment. For the cases of extreme condition with 4 compartments flooded, Case 5 supposes that four aft compartments including the diesel engine room were

flooded, while the steering gear room remains intact, and Case 6 included the steering gear room as one of the four flooded compartments.

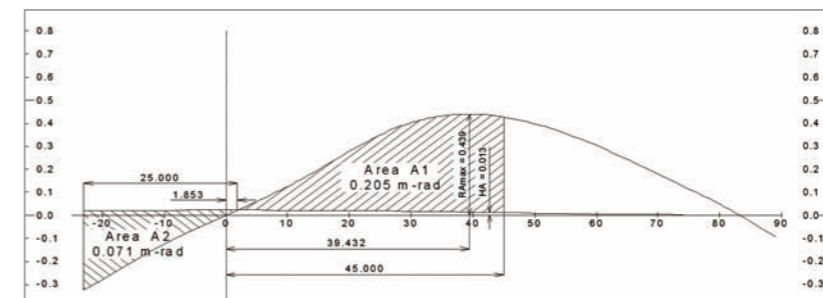
2) Damage Stability Assessment with 2 Compartments Flooded

(1) Case 1: 2 Compartments Damaged(Diesel Engine Room and Gas Turbine Room Flooded)

As shown in 〈Figure Appendix VI-4-1〉, it is possible to stay afloat with the diesel engine room and gas turbine room flooded. The stability curve for this case is shown in 〈Figure Appendix VI-4-2〉, and the results are summarized in 〈Table Appendix VI-4-2〉. The standards such as initial inclining angle, capsizing force vs. stability ratio(A1/A2), stability(A1), maximum residual righting arm(RA_{max}-HA), and the margin line are all satisfied after the damage. Hence, the stability level with the diesel engine and gas turbine room inundated suffices the standards.



〈Figure Appendix VI-4-1〉 Buoyancy level with 2 compartments flooded(Case 1)



〈Figure Appendix VI-4-2〉 Dynamic stability curve with the damage

Category	Design standard	ROKS Cheonan	Result
Initial inclining angle after the damage	Below 15°	0°	Sufficient
Capsizing force vs. stability ratio(A1/A2)	Below 1.4	2.887	Sufficient
Stability(A1)	Above 0.024 m · rad	0.205 m · rad	Sufficient
Max residual righting arm(RAmax-HA)	Above 0.075m	0.192m	Sufficient
Margin line ²⁰⁾	Located above waterline	1.545m	Sufficient

〈Table Appendix VI-4-2〉 Stability analysis results of Case 1

(2) Case 2: 2 Compartments Damaged(Diesel Engine Room & 1 Aft Compartment Flooded)

The buoyancy level estimation result with the diesel engine room and one adjacent aft compartment flooded is depicted in 〈Figure Appendix VI-4-3〉, and it indicates that buoyancy is achieved. The stability estimation results are summarized in 〈Table Appendix VI-4-3〉. The standards such as initial inclining angle after the damage, capsizing force vs. stability ratio(A1/A2), stability(A1), maximum residual righting arm(RAmax-HA), and the margin line are all met. Therefore, the stability level of flooding in the diesel engine room and one adjacent aft compartment satisfies the design standards.



〈Figure Appendix VI-4-3〉 Buoyancy level with 2 compartments flooded(Case 2)

Category	Design standard	ROKS Cheonan	Result
Initial inclining angle after damage	Below 15°	0°	Sufficient

.....
20) Margin line: 76mm line below the main deck side, and must be above waterline.

Capsizing force vs. stability ratio(A1/A2)	Above 1.4	2.913	Sufficient
Stability(A1)	Above 0.024 m · rad	0.201 m · rad	Sufficient
Max residual righting arm(RAmax-HA)	Above 0.075m	0.424m	Sufficient
Margin line	Located above waterline	1.689m	Sufficient

〈Table Appendix VI-4-3〉 Stability analysis results of Case 2

3) Damage Stability Assessment with 3 Compartments Flooded

(1) Case 3: 3 Compartments Damaged(Diesel Engine Room & 2 Aft Compartments)

As the design standard for ROKS Cheonan upon inundation of two compartments was sufficiently fulfilled, analysis on stability and buoyancy level was conducted for conditions where three compartments flooded including the diesel engine room and 2 adjacent aft compartments. The result on buoyancy level is displayed on 〈Figure Appendix VI-4-4〉, and buoyancy would be maintained with the main deck hatch closed. The stability computation results are as shown in 〈Table Appendix VI-4-4〉. The initial inclining angle after the damage, capsizing force vs. stability ratio(A1/A2), stability(A1), and the maximum residual righting arm(RAmax-HA) are sufficiently contented. The margin line standard was assessed to be unfulfilled, but this only indicates that the aft end of the stern shown in 〈Figure Appendix VI-4-4〉, may submerge a little and gradual flooding would occur if the main deck hatch remained open, but if it was closed, buoyancy would be maintained without additional flooding. Therefore, it can be concluded that while a partial submerging of the stern could occur, the stability is still retained, hence, it is possible for the buoyancy level to be stably maintained for an extended period of time.



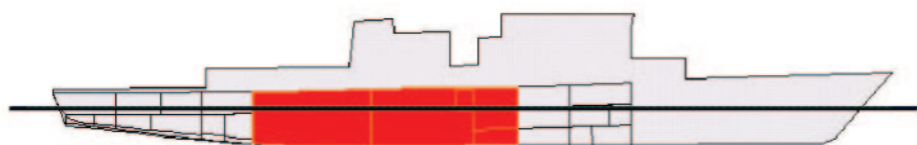
〈Figure Appendix VI-4-4〉 Buoyancy level with three compartments flooded(Case 3)

Category	Design standard	ROKS Cheonan	Result
Initial inclining angle after damage	Below 15°	0°	Sufficient
Capsizing force vs. stability ratio(A1/A2)	Above 1.4	3.040	Sufficient
Stability(A1)	Above 0.024 m · rad	0.076 m · rad	Sufficient
Max residual righting arm(RA _{max} -HA)	Above 0.075m	0.163m	Sufficient
Margin line	Located above waterline	-0.627m	Insufficient

〈Table Appendix VI-4-4〉 Stability analysis results of Case 3

(2) Case 4: 3 Compartments Damaged(Diesel Engine Room, Gas Turbine Room, 1 Compartment in front of the Gas Turbine Room)

As one of the cases beyond the design standard(two compartments flooded), analyses of stability and buoyancy level were conducted with an assumption of three compartments flooded including the machinery room, gas turbine room and one compartment in front of the gas turbine room. The result of buoyancy level calculation is depicted in 〈Figure Appendix VI-4-5〉, and it shows buoyancy could be maintained. The calculated stability results are summarized in 〈Table Appendix VI-4-5〉. The initial inclining angle after the damage, capsizing force vs. stability ratio(A1/A2), stability(A1), max residual righting arm(RA_{max}-HA), and the margin line standards are sufficiently satisfied. Consequently, with three compartments(diesel engine room, gas turbine room, and one compartment in front of the gas turbine room) flooded, the stability level remains stable.



〈Figure Appendix VI-4-5〉 Buoyancy level with 3 compartments flooded(Case 4)

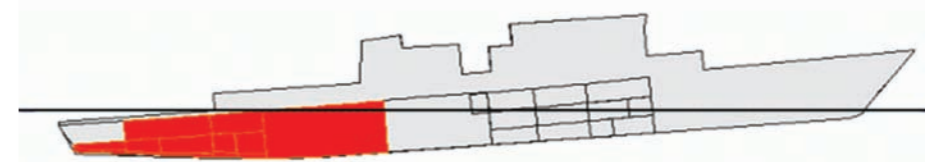
Category	Design standard	ROKS Cheonan	Result
Initial inclining angle after damage	Below 15°	0°	Sufficient
Capsize vs. stability ratio(A1/A2)	Above 1.4	2.724	Sufficient
Stability(A1)	Above 0.024m · rad	0.158m · rad	Sufficient
Max residual righting arm(RA _{max} -HA)	Above 0.075m	0.318m	Sufficient
Margin line	Located above waterline	1.048m	Sufficient

〈Table Appendix VI-4-5〉 Stability analysis results of Case 4

4) Damage Stability Assessment with 4 Compartments Flooded

(1) Case 5: 4 Compartments Damaged(4 Aft Compartments including the Diesel Engine Room Flooded, except the Steering Gear Room)

As one of the cases which are way beyond the design standard(2 compartments flooded), analyses of stability and buoyancy level were conducted supposing four compartments flooded(without steering gear room), including the diesel engine room. The calculation result on the buoyancy level is shown to 〈Figure Appendix VI-4-6〉. It indicates that the buoyancy is achieved if the main deck hatch was closed. The stability computation results are summarized in 〈Table Appendix VI-4-6〉. The initial inclining angle after the damage, capsizing force vs. stability ratio(A1/A2), stability(A1), maximum residual righting arm(RA_{max}-HA) are sufficient to qualify the standards, therefore, stability would be maintained. The margin line standard is assessed to be insufficient, but this indicates that while the aft end of the stern shown in 〈Figure Appendix VI-4-6〉 may submerge due to gradual flooding if the main deck hatch remained open, but buoyancy could be achieved if it was closed. To summarize, a partial submerging of the stern could occur, but stability is still retained, hence, buoyancy level will be maintained for a long duration of time.



〈Figure Appendix VI-4-6〉 Buoyancy level with four compartments flooded(Case 5)

Category	Design standard	ROKS Cheonan	Result
Initial inclining angle after damage	Below 15°	0°	Sufficient
Capsize vs. stability ratio(A1/A2)	Above 1.4	2.871	Sufficient
Stability(A1)	Above 0.024 m · rad	0.089 m · rad	Sufficient
Max residual righting arm(RAmax-HA)	Above 0.075m	0.187m	Sufficient
Margin line	Located above waterline	-0.758m	Insufficient

〈Table Appendix VI-4-6〉 Stability analysis results of Case 5

(2) Case 6: 4 Compartments Damaged(4 Aft Compartments including the Diesel Engine and Steering Gear Room Flooded)

As one of the cases well beyond the design standard(two compartments flooded), analyses on stability and buoyancy level were conducted with four compartments flooded including the diesel engine room and steering gear room. The stability computation results are summarized in 〈Table Appendix VI-4-7〉. Despite the fact that the initial inclining angle level was satisfied, capsizing force vs. stability ratio(A1/A2), stability(A1), maximum



〈Figure Appendix VI-4-7〉 Buoyancy level with four compartments flooded(Case 6)

Category	Design standard	ROKS Cheonan	Result
Initial inclining angle after damage	Below 15°	0°	Sufficient
Capsize vs. stability ratio(A1/A2)	Above 1.4	2.871	Sufficient
Stability(A1)	Above 0.024 m · rad	0.089 m · rad	Sufficient
Max residual righting arm(RAmax-HA)	Above 0.075m	0.187m	Sufficient
Margin line	Located above waterline	-0.758m	Insufficient

〈Table Appendix VI-4-7〉 Stability analysis results of Case 6

residual righting arm(RAmax-HA), and the margin line levels were all turned out to be insufficient. Hence, the hull would lose its buoyancy level and completely sink with the time passing.

5. Stability of the Bow and Stern after Separation

An ordinary stability design for a vessel analyzes the stability prior and posterior to the damage, while the damage dealt here only implies flooding, not a separation. However, ROKS Cheonan was split and separated centering around the gas turbine room, after which the stern sunk shortly, and lastly the bow sunk after being capsized in 90 degrees to the starboard side. In order to technically specify the circumstances regarding the sinking, stabilities after the separation of the bow and stern was also analyzed.

1) Stability of the Bow and Stern Immediately After Separation

The stability characteristics of the bow and stern after the separation of the ship are listed in 〈Table Appendix VI-5-1〉. G' in the table indicates the new center of gravity to which the original center G has migrated according to the volume change of loaded fluids(e.g.: fuel). Therefore, the stability assessment index $G'M = KM - KG - GG'$.

In 〈Table Appendix VI-5-1〉, the G'M of the bow section is calculated to be a negative value of -0.02m. Thus, any minuscule external force such as wind or wave to the sep-

Category	Bow section	Stern section
Displacement	664 tons	559 tons
KG	4.347m	3.515m
KM	4.425m	5.903m
KB	2.420m	2.346m
GG'	0.098m	0.036m
G'M	-0.020m	2.35m

〈Table Appendix VI-5-1〉 Initial stabilities of the bow and stern after the separation

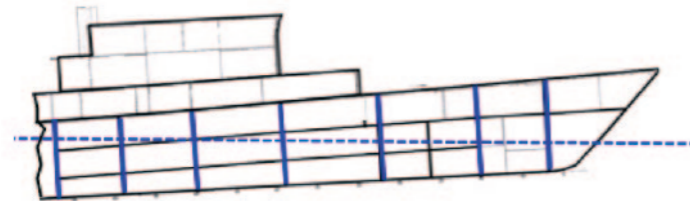
arated bow could cause the ship to lose its stability and thus capsize. The capsizing direction would correspond to the direction of the external force. In conclusion, the bow section loses its stability after the separation, due to the elevated center of gravity.

The G'M of the stern section is calculated to be 2.35m. Hence, the stern section is estimated not to have capsized immediately after the separation.

2) Buoyancy Assessments of the Bow and Stern after Separation

(1) Buoyancy Assessment of the Bow

Right after the separation, the buoyancy level of the bow section before the capsizing is analyzed and displayed in <Figure Appendix VI-5-1>. Since there was no stability on the bow section with the GM value of -0.02m, it is assessed that the ship would have capsized to the starboard direction as the explosion force was exerted from the portside bottom. It is analyzed that the separated bow, having seven compartments, would have experienced gradual flooding. Therefore, it would have been able to maintain buoyancy for some period of time while being capsized; however, due to continued influx of seawater through the entrance and the ventilator, the ship sank eventually.



<Figure Appendix VI-5-1> Estimation of the bow buoyancy level immediately after the separation

(2) Buoyancy Assessment of the Stern

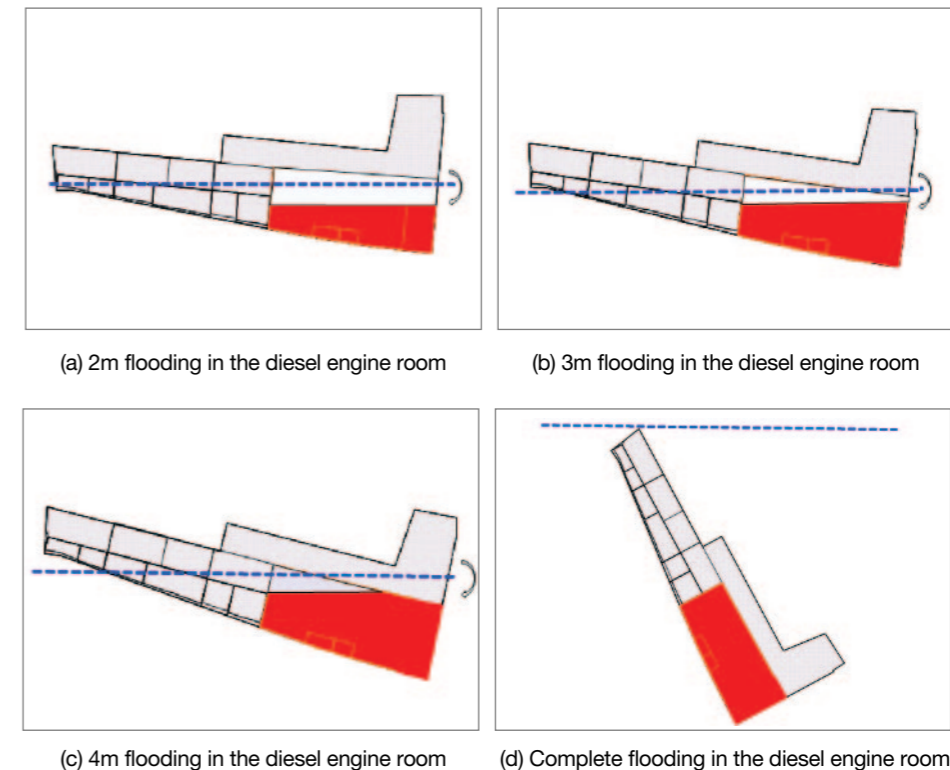
The buoyancy level of the stern section immediately after the separation is estimated and displayed in <Figure Appendix VI-5-2>. With GM value of 2.35m, it is estimated that its stability was retained with no capsizing.

The separated stern section consisted of four watertight compartments, and especially it contained the diesel engine room occupying 40% of the stern volume; thus, flooding of the diesel engine room would have had a significant impact on the buoyancy



<Figure Appendix VI-5-2> Estimation of the stern buoyancy level immediately after the separation

level of the stern. First, the posture and buoyancy level of the ship were analyzed in accordance with different flooding conditions in the diesel engine room to substantiate the sinking process of the stern. If compartments other than the damaged diesel engine room were completely sealed, buoyancy retention would have been possible until the damaged diesel engine room was flooded up to 4m, and in case of complete flooding in the diesel engine room, the ship would have sunk. The buoyancy level estimations on each of the conditions are depicted in <Figure Appendix VI-5-3>.



<Figure Appendix VI-5-3> Buoyancy level estimations with each flooding condition in the diesel engine room

The details of the time and posture regarding the sinking of the stern have also been analyzed. The actual damage status of the stern was taken into consideration during the analysis. The initial inflow of seawater to the diesel engine room is depicted in (Figure Appendix VI-5-4). It commenced from the watertight bulkhead between the diesel engine room and gas turbine room through the crater created by the splitting of the shaft connecting the gas turbine and reduction gear, as well as from the hatch on the upper portion of the diesel engine room used for installing diesel engine on the main deck and generator on the stack. The second inflow occurred from the opened watertight doors along the main passageway; the doors were open since ROKS Cheonan was under normal operating condition. Eventually, the overflow of seawater propagated from the diesel engine room to the

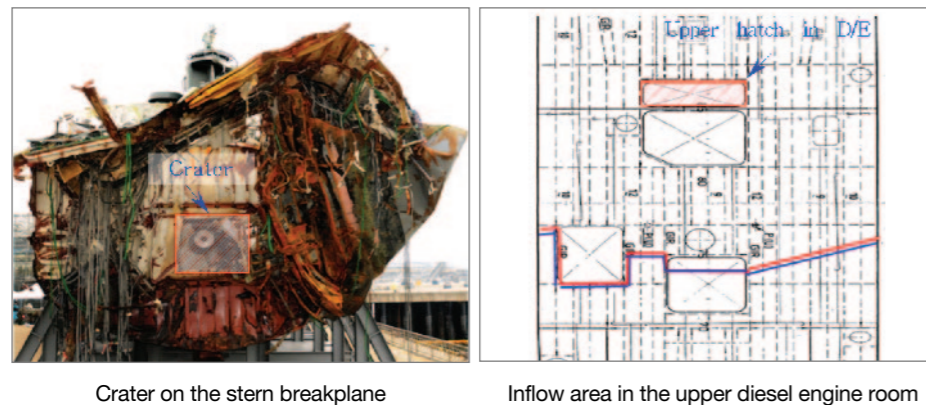


(Figure Appendix VI-5-4) Crater on the stern breakplane & the main deck hatch

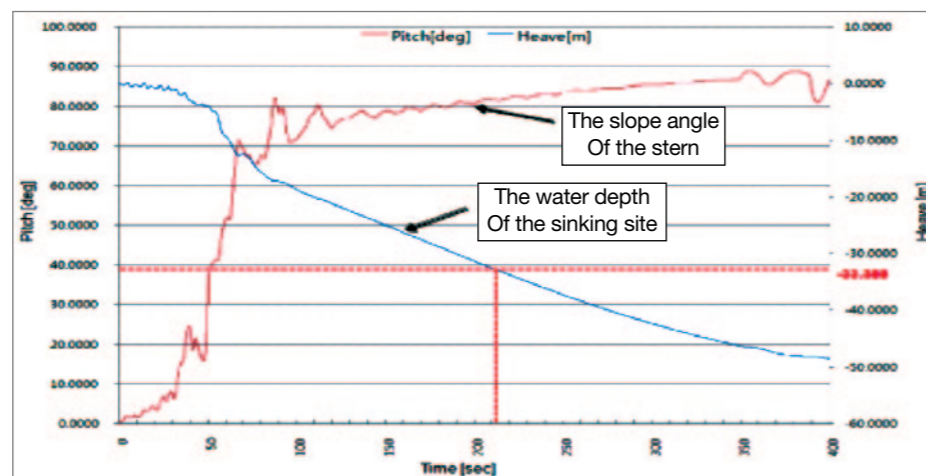


(Figure Appendix VI-5-5) Sinking time estimation of the stern

aft compartments.

A time elapse analysis of the stern sinking is shown in (Figure Appendix VI-5-5). Since 90 seconds after the separation of the hull, as the diesel engine room became flooded, the ship inclined in 80 degree angle, and from 210 seconds, more than the length of the stern section, 33.4m, had submerged. Although differences may exist in flooding volume due to the equipped structures in the machinery room, a complete sinking would have occurred at least after 200 to 250 seconds.

3) Sub-conclusion

The stability design standard of ROKS Cheonan prior to the damage was much stricter than that of a merchant vessel at the time of its construction, and was assessed to possess basic stability twice as strong compared to the merchant vessel standard. As for protection from damages, it was designed to endure two, three, and even four compartments flooded as long as the steering gear room remains intact.

In regard of the separation centering around the gas turbine room as a center, it is analyzed that the buoyancy level of the stern would have been maintained as long as the bulkhead between the gas turbine room and diesel engine room is not damaged and kept watertight; however, in the actual incident, rapid inflow occurred through the crater on the watertight bulkhead between the diesel engine room and gas turbine room as well as around the stack on the main deck and the upper diesel engine room, leading the ship to sink completely 200 - 250 seconds after the separation.

The separated bow would have lost its stability immediately due to the negative stability ($GM < 0$). After the split, any minuscule external force such as wind or wave would have been sufficient to capsize the bow. It would have been capsized toward the starboard direction as a result of the external force exerted on the portside. However, considering the bow was divided into seven compartments it would have been able to maintain buoyancy for a significant duration of time after the separation, followed by capsize, and sinking because of the continuous inflow of seawater through the entrance and ventilator.

Appendix VII. Basic Hull Strength Analysis Result

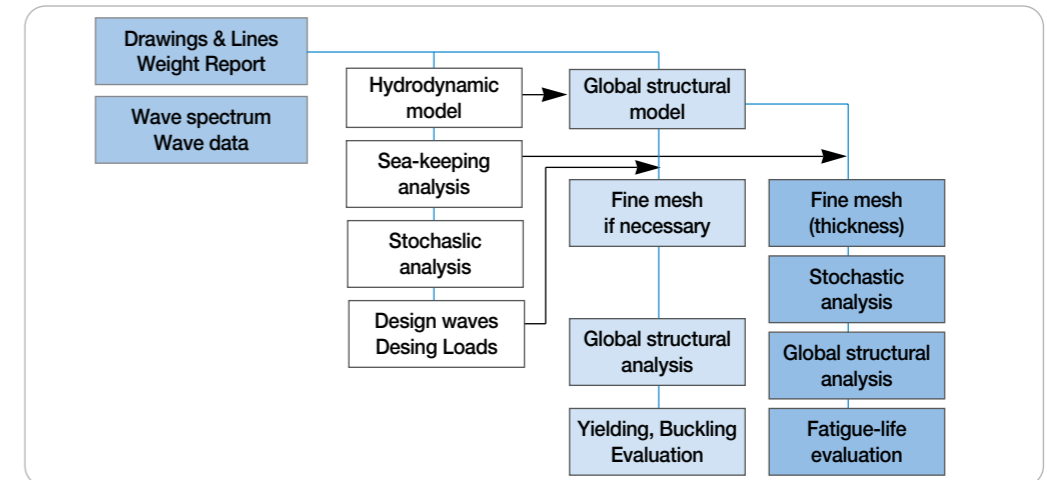
1. Objective

At the time of its design, ROKS Cheonan was designed based on the structural design standard of US Navy, Structural Design Manual for Naval Surface Ship(1974). However, the structural safety of ROK Navy vessels nowadays are being validated in accordance with the direct strength analysis which is based upon the shipbuilding design technology of ROK. By carrying out the direct strength analysis on the structure of a ROKS Cheonan class warship, which was designed in accordance with US Navy standard of 1974, the structural stability of ROKS Cheonan was assessed on the basis of contemporary standard. The verification of basic structural safety is a fundamental procedure which comes before the damage analysis, and is conducted in order to evaluate the basic strength which is required to execute a destruction factor analysis.

2. Flow Chart of Direct Strength Analysis

The direct strength analysis calculates the motion and load of a ship against waves, estimates with the most probable extreme load which a ship could undergo within its lifetime of 25 to 30 years by a stochastic and statistical method, and then determines the design wave for generating the extreme load. It then conducts a structural analysis by loading a 3D structure model for the whole ship, and evaluates the structural safety(See <Figure Appendix VII-2-1>).

As demonstrated in <Figure Appendix VII-2-1>, the most recent direct strength analysis procedure includes fatigue life evaluation. However, since the direct strength analysis of ROKS Cheonan was conducted not for a designing purpose, but for analysis of damage factors, and because fatigue failure already turned out not to be the cause of the sinking, the fatigue life evaluation was excluded from the analysis.

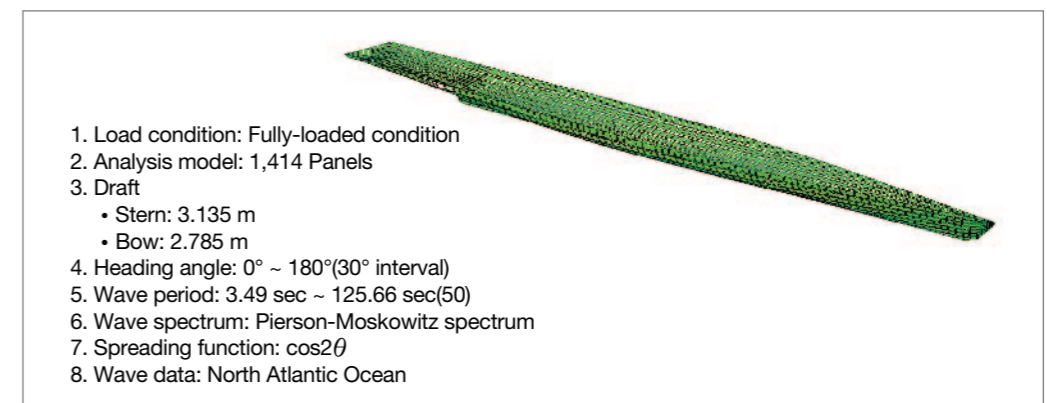


<Figure Appendix VII-2-1> Direct strength analysis flow chart

3. Hydrodynamic Analysis

1) Hydrodynamic Analysis Modeling

The analysis model for the wave load estimation of ROKS Cheonan includes a detailed modeling of the hull section below the waterplane to effectively delineate the shape of the ship and pressure distribution. <Figure Appendix VII-3-1> illustrates the 3D model and the load condition used for the wave load estimation. Additionally, the loads were distributed along the hull under an assumption of a fully-loaded condition.



<Figure Appendix VII-3-1> 3D hydrodynamic analysis model and load condition

2) Design Wave Selection

The design waves for basic strength analysis were selected as shown in <Table Appendix VII-3-1>, and these design waves assume the most intensive loading that the ship may experience with a probability of 10^{-8} , while operating on the most severely conditioned sea, Northern Atlantic Ocean, during 25~30 years of its navigation.

- Design wave maximizing wave vertical bending moment affecting the center of the ship.
- Design wave maximizing wave horizontal bending moment affecting the center of the ship.
- Design wave maximizing torsion moment affecting the center of the ship.
- Design wave maximizing vertical acceleration at the bow.
- Design wave maximizing pressure on the center waterplane of the ship.

Design load	Heading angle	Wave length	Design value	Design wave height
Vertical bending moment	180°	65.37m	83,824kN·m	10.60m
Horizontal bending moment	120°	43.81m	18,722kN·m	4.53m
Torsion moment	60°	65.37m	13,757kN	8.55m
Vertical acceleration	120°	48.75m	14.71m/sec ²	6.92m
Pressure	90°	34.24m	75.92kPa	6.67m

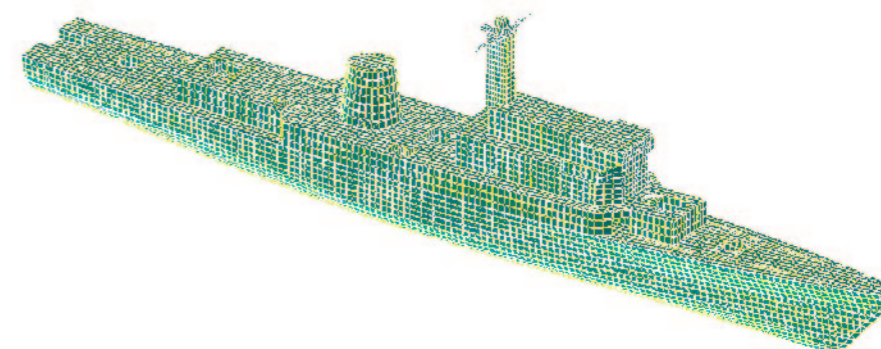
<Table Appendix VII-3-1> Design wave estimation results of ROKS Cheonan to conduct the direct strength analysis

4. Structural Analysis

1) Structural Analysis and Allowable Stress Standard

The range of finite element model for structural analysis included every structure on the ship such as the superstructures, the stack, and the mast set up along the full width and length of the ship. The evaluation of the main hull structure, which was composed of mild steel, was based on the allowable stress standard employed in the ROK Navy design/con-

struction standard. The structural analysis result on the superstructures, which are composed of aluminium, was based on the allowable stress standard from Korean Register of Shipping in its rules for a high speed craft.



<Figure Appendix VII-4-1> 3D structural analysis model

Mild Steel	Yield Stress(σ _Y)	Allowable stress(σ _e)	AL 5083, H116	Yield Stress(σ _Y)	Allowable stress(σ _e)
Longi. Member	235 MPa	200 MPa	Longi. Member	215 MPa	127 MPa
Trans. Member	235 MPa	177 MPa	Trans. Member	215 MPa	

<Table Appendix VII-4-1> Allowable stress of main hull structure

<Table Appendix VII-4-2> Allowable strength of superstructure

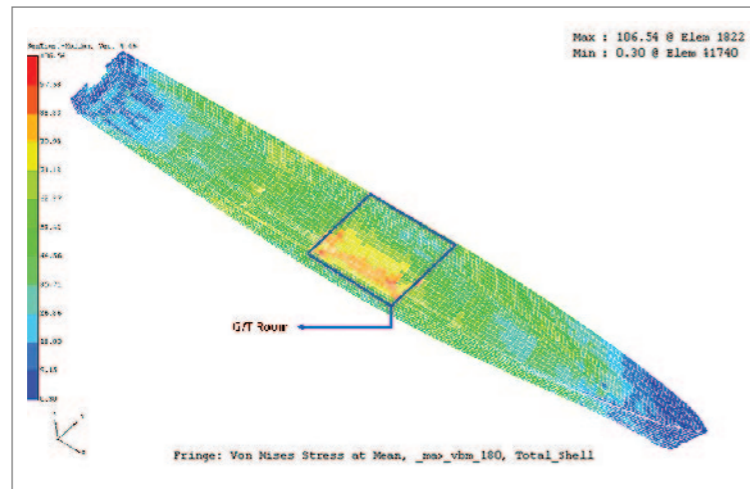
2) Structural Analysis Result and Evaluation

The direct strength analysis was carried out for each design wave(ones that maximize the vertical bending moment, horizontal bending moment, torsion moment, and the vertical acceleration respectively) which generates maximum loadings, using the maximum values of allowable stress for each structural member. The result of the direct strength analysis for every design wave showed that the vertical bending moment was the dominating load factor for ROKS Cheonan. Consequently, only the results of vertical bending moments are provided below.

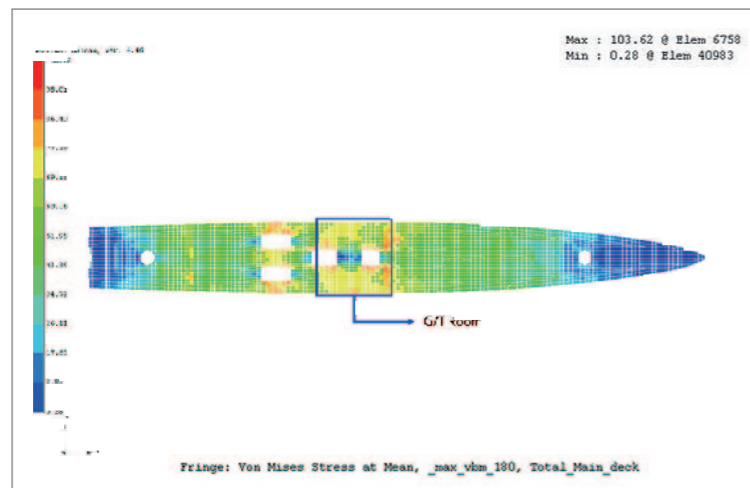
(1) Yield Strength Assessment

The analysis results for the main structures, including the shell and main deck, are pro-

vided in <Figure Appendix VII-4-2> and <Figure Appendix VII-4-3>. <Table Appendix VII-4-3> compares the maximum generated stress on the major longitudinal members such as main deck, shell plate as well as the bulkheads, web frames, and the superstructures with the allowable stress. As described in <Table Appendix VII-4-3>, the stress generated on every structural member is below their allowable stress levels. Especially, the stress on the major structural members is, at maximum, around 50% of the standard values, well sufficing the yield strength assessment standard.



<Figure Appendix VII-4-2> Structural analysis result of the shell plates



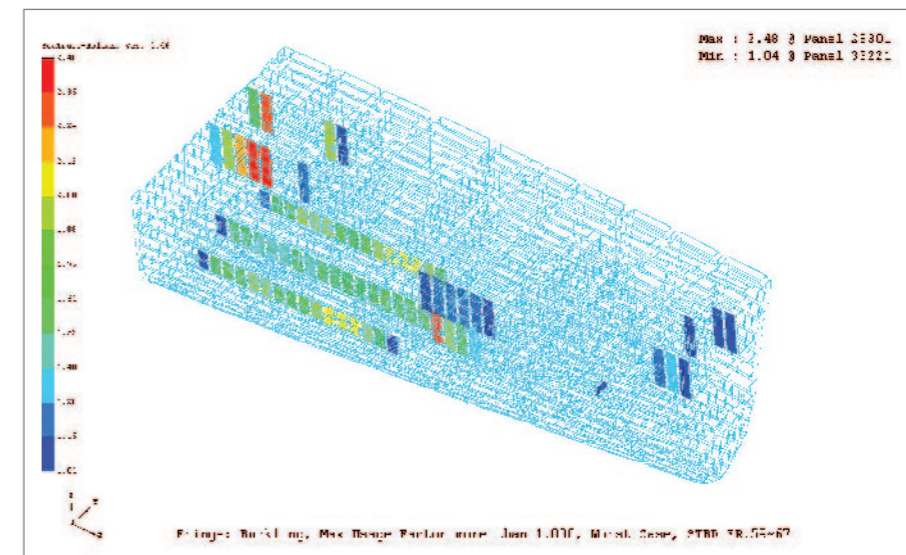
<Figure Appendix VII-4-3> Structural analysis of the main deck

Members	Material	Allowable stress(MPa)	Possible maximum stress(MPa)	Remarks
O-2 Deck	AL ²¹⁾	127	20.0	16% Sufficient
O-1 Deck	AL	127	77.6	61% Sufficient
Main deck	MS ²²⁾	200	103.62	52% Sufficient
1st Platform deck	MS	200	42.14	21% Sufficient
2nd Platform deck	MS	200	44.84	22% Sufficient
Shell	MS	200	106.54	53% Sufficient
FR. 39 BHD	MS	177	52.8	30% Sufficient
FR. 77 Web frame	MS	177	152	86% Sufficient

<Table Appendix VII-4-3> Stress evaluation of each structural member

(2) Buckling Strength Assessment

For the buckling strength assessment of ROKS Cheonan, an analysis method based on the ship design/construction standard(steel) was applied. The representative buckling strength assessment results on the compressive stress and the breaking stress affecting plates of major structural members(derived by using stress estimates from hull structure analysis) are listed in <Figure Appendix VII-4-4>, <Figure Appendix VII-4-5> and <Figure Appendix



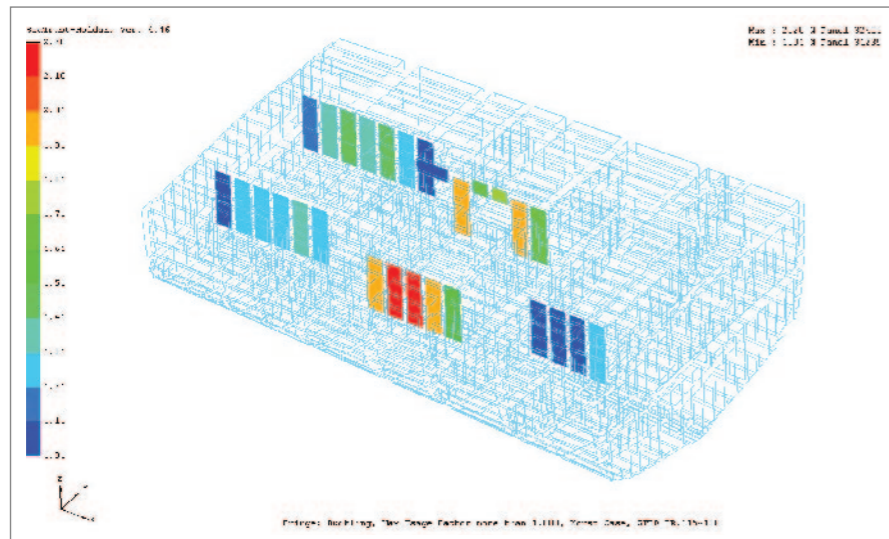
<Figure Appendix VII-4-4> Buckling strength assessment result: FR. 27 ~ FR. 67

21) AL: Aluminum.
22) MS: Mild Steel.

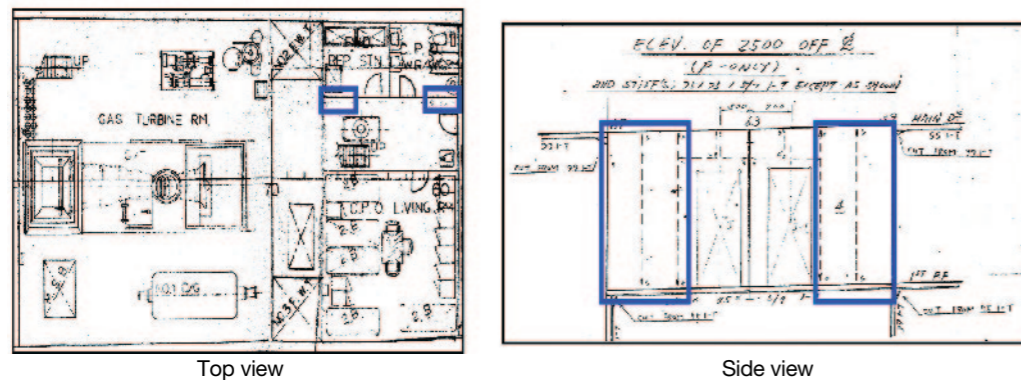
VII-4-6). Based on the result of the analysis, while there was no possibility of buckling at the central region of the hull, one at partial longitudinal bulkhead was assessed possible. However, these bulkheads are structures for sectioning each compartment, and therefore, do not affect the hull girder strength. An example of longitudinal bulkhead for sectioning compartments is provided in <Figure Appendix VII-4-6>.

5. Analysis Result

Based on the result of the direct strength analysis regarding the maximum design waves (wave height 10.6m), with extreme loads on the hull, and during the ship lifetime of 25-30 years, it was found that ROKS Cheonan sufficiently satisfies the yield strength standard. Although there is a possibility of buckling in some bulkheads on the stern and the bow, these partial bulkheads are sectioning members, and hence would not affect the hull girder strength as non-resistant bulkheads. Therefore, excluding the possibility of extraordinary conditions such as an external attack, it is analyzed that ROKS Cheonan possessed sufficient structural strength.



<Figure Appendix VII-4-5> Buckling strength assessment result: FR.106 ~ FR.130



<Figure Appendix VII-4-6> Location and shape of partial longitudinal bulkhead(example)

Joint Investigation Report
On the Attack Against ROK Ship Cheonan

Copyright © 2010 by the Ministry of National Defense
of the Republic of Korea

Published by Myungjin Publication Inc.

The first print date of the first edition_ September 10, 2010

Sales Contact_ (Tel.) 82-2-326-0026

ISBN 978-89-7677-711-9 03300

Price written on the back cover.

Damaged copies can be exchanged with new ones.